Geophys. J. Int. (2006) **167,** 106–126 doi: 10.1111/j.1365-246X.2006.02949.x

P- and *S*-velocity images of the lithosphere–asthenosphere system in the Central Andes from local-source tomographic inversion

Ivan Koulakov,[1,2] Stephan V. Sobolev[1,3] and Günter Asch[1]

[1] *GeoForschungZentrum-Potsdam, Germany. E-mail: ivank@gfz-potsdam.de*
[2] *Institute of Geology, SB RAS, Novosibirsk, Russia*
[3] *Institute of Physics of the Earth, RAS, Moscow, Russia*

Accepted 2006 February 6. Received 2006 January 24; in original form 2004 December 16

SUMMARY

About 50 000 *P* and *S* arrival times and 25 000 values of t^* recorded at seismic arrays operated in the Central Andes between 20°S and 25°S in the time period from 1994 to 1997 have been used for locating more than 1500 deep and crustal earthquakes and creating 3-D *P*, *S* velocity and *Qp* models. The study volume in the reference model is subdivided into three domains: slab, continental crust and mantle wedge. A starting velocity distribution in each domain is set from *a priori* information: in the crust it is based on the controlled sources seismic studies; in slab and mantle wedge it is defined using relations between *P* and *S* velocities, temperature and composition given by mineral physics. Each iteration of tomographic inversion consists of the following steps: (1) absolute location of sources in 3-D velocity model using *P* and *S* arrival times; (2) double-difference relocation of the sources and (3) simultaneous determination of *P* and *S* velocity anomalies, *P* and *S* station corrections and source parameters by inverting one matrix. Velocity parameters are computed in a mesh with the density of nodes proportional to the ray density with double-sided nodes at the domain boundaries. The next iteration is repeated with the updated velocity model and source parameters obtained at the previous step. Different tests aimed at checking the reliability of the obtained velocity models are presented. In addition, we present the results of inversion for *Vp* and *Vp/Vs* parameters, which appear to be practically equivalent to *Vp* and *Vs* inversion. A separate inversion for *Qp* has been performed using the ray paths and source locations in the final velocity model. The resulting *Vp*, *Vs* and *Qp* distributions show complicated, essentially 3-D structure in the lithosphere and asthenosphere. *P* and *S* velocities appear to be well correlated, suggesting the important role of variations of composition, temperature, water content and degree of partial melting.

Key words: Central Andes, mantle wedge, seismic tomography, subduction.

1 INTRODUCTION

The Andes are one of the largest active mountain ranges in the world, extending for over 8000 km along the western edge of South America (Fig. 1). The subduction of the Nazca plate at a rate of about 8.4 cm yr^{-1} (relative to South America (DeMets *et al.* 1990)) under the South American continent has been going on for more than 200 Myr. In spite of such a long subduction history, the main orogenic processes that resulted in building high mountain chain (up to 6000 m of altitude) took place only during the last 20 Ma. The reason of such strong activation during the recent time is still debated. The shape of the subducted plate in the Central Andes (between 20°S and 26°S of latitude) is fairly well constrained down to the depth of 250 km from different observations. The local seismicity distributions in the Wadati-Benioff zone and results of the deep seismic reflection studies (e.g. Patzwahl *et al.* 1999) show that the subducted Nazca plate dips at the angle of ∼20° down to a depth of 50 km. At greater depths the dip angle increases.

The crustal structure of the Central Andes was influenced by the eastward-migrating magmatic arc (Scheuber *et al.* 1994) due to strong erosion of the upper plate lithosphere in the subduction zone. This migration is expressed by a 200 km shift of the volcanic arc system to the east since the early Jurassic. Today the main volcanic arc is located along the Western Cordillera. The forearc region can be subdivided into four main morphological units from west to east (Fig. 1):

(1) coastal Cordillera coinciding with position of volcanic arc in Jurassic times;

(2) the Longitudinal Valley located at the place of the Jurassic back arc basin and the Mid-Cretaceous magmatic arc;

(3) Precordillera located on the Late Cretaceous magmatic arc and

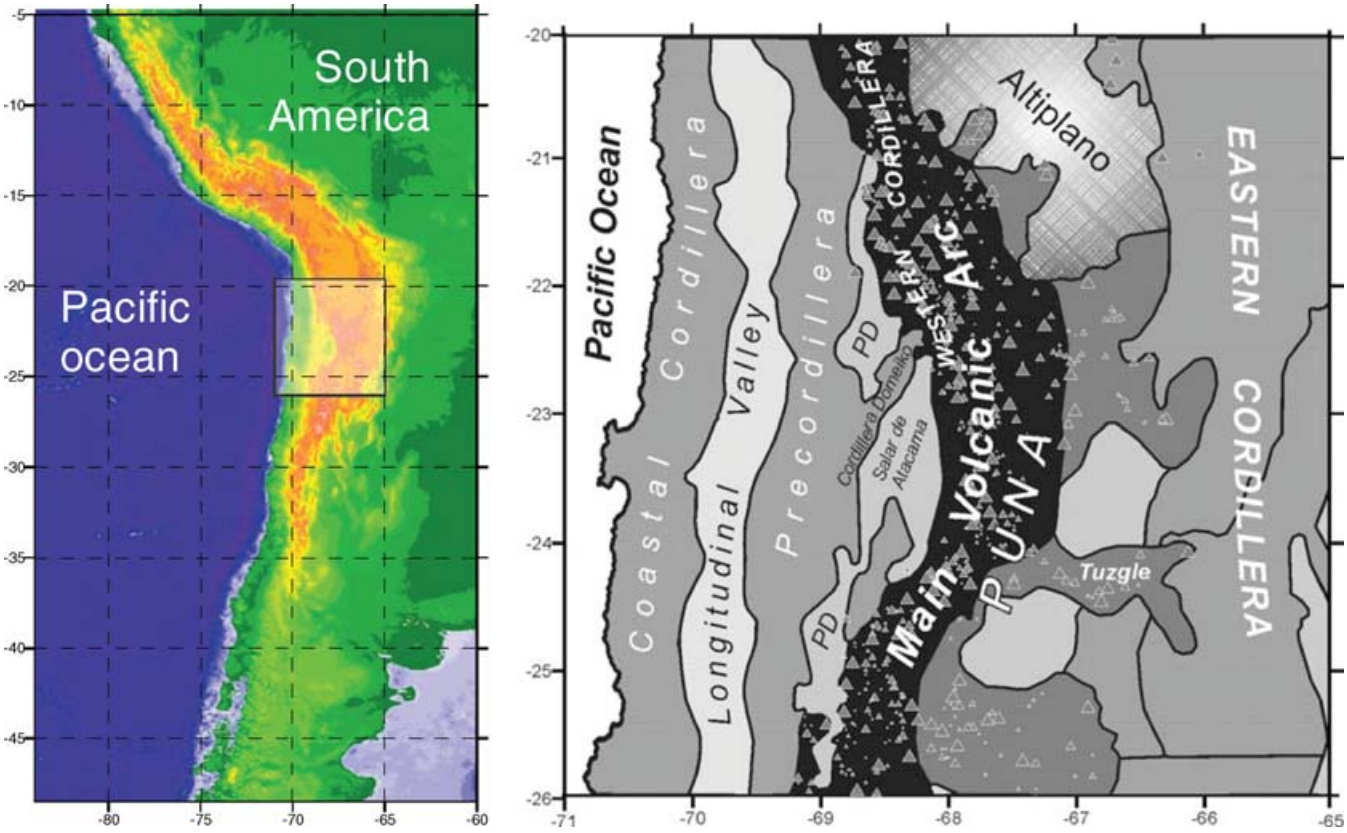

Figure 1. Position of the study region (left) and simplified map of the main tectonic elements (right). PD: Preandean depression; APVC: Altiplano-Puna volcanic complex. Position of recent volcanoes (up to 5 Ma) from the catalogue by de Silva & Francis (1991) is shown by triangles. Size of the triangles reflects volume of the volcanoes.

(4) the Preandean depression containing the Salar Atacama block and bordered from the east by active volcanoes.

Geophysical (Wigger *et al.* 1994; Beck *et al.* 1996; Yuan *et al.* 2000, 2002) and geochemical (e.g. Worner *et al.* 1992) observations reveal elevated crustal thickness of about 50–70 km or more in the Central Andes. In the Eastern Cordillera the thick crust is probably entirely related to the crustal doubling due to the tectonic shortening (Schmitz 1994). In the arc and forearc regions also magmatic addition and/or hydrated mantle might contribute to the crustal thickening (Giese *et al.* 1999; Graeber & Asch 1999). However, our knowledge of the upper mantle and deep crustal structure remains too sparse to quantify these processes. The actual work aims at providing the quantitative constraints, which would help to better understand the crustal thickening and mountain building processes in the Central Andes during the last 20 Ma. Although we will also discuss interpretation of the results of tomographic inversion, the main attention of this paper is the methodological aspects of the algorithm and analysis of the reliability of the tomographic images.

1.1 Previous seismological studies

The Central Andes have been the subject of vigorous research in most of the geological and geophysical domains. Different scale seismological experiments have been performed during the last decade. 2-D structure of the subduction zone between 20°S and 25°S has been studied with active source near vertical reflection (ANCORP Group 1999, 2003) and wide-angle seismic methods (e.g. Patzwahl *et al.* 1999; ANCORP Group 2003). The lithospheric and the mantle structures in the central Andes has been investigated with the body waves tomography (Graeber & Asch 1999; Husen *et al.* 2000; Myers *et al.* 1998; Dorbath *et al.* 1993; Dorbath & Masson 2000; Schurr 2001; Schurr *et al.* 2003), attenuation tomography (Haberland & Rietbrock 2001; Haberland *et al.* 2003; Schurr *et al.* 2003), surface wave tomography (Baumond *et al.* 1999, 2002; Swenson *et al.* 2000). The structure of the main interfaces and anisotropy of the uppermost mantle have been studied with the use of receiver function analysis (Beck & Zandt 2002; Yuan *et al.* 2000, 2002; Leidig & Zandt 2003). In the framework of the multidisciplinary international project SFB 267 (1994–1997) several arrays of portable seismic stations were installed between 20°S and 25°S from the Pacific coast across the Andean mountain range (Fig. 2a). The *P* and *S* arrival times and first motions polarities were handpicked (Rietbrock & Scherbaum 1998; Schurr 2001) and used for preliminary location of the local seismicity (Fig. 2b). The accuracy of picking is fairly high: for *P* arrival times it is estimated as 0.04 s, for *S* picks it is significantly lower, 0.5 s (Schurr 2001). In general, about 1500 of deep and crustal earthquakes were located on the basis of about 50 000 rays recorded by the arrays in the Central Andes. This information was used to study the velocity structure under the Central Andes (Schurr *et al.* 1999; Schurr 2001). Schurr *et al.* (1999) employed the method of joint inversion of 1-D structure and localization of sources (Kissling *et al.* 1994; Husen *et al.* 2000) and computed a 1-D reference model providing minimal residuals. Starting from this model Schurr (2001) and Schurr *et al.* (2003) performed an iterative tomographic inversion and computed models of *P*-velocity anomalies, *Vp/Vs* ratio variations, and variations of *P*-wave attenuation *Q*.

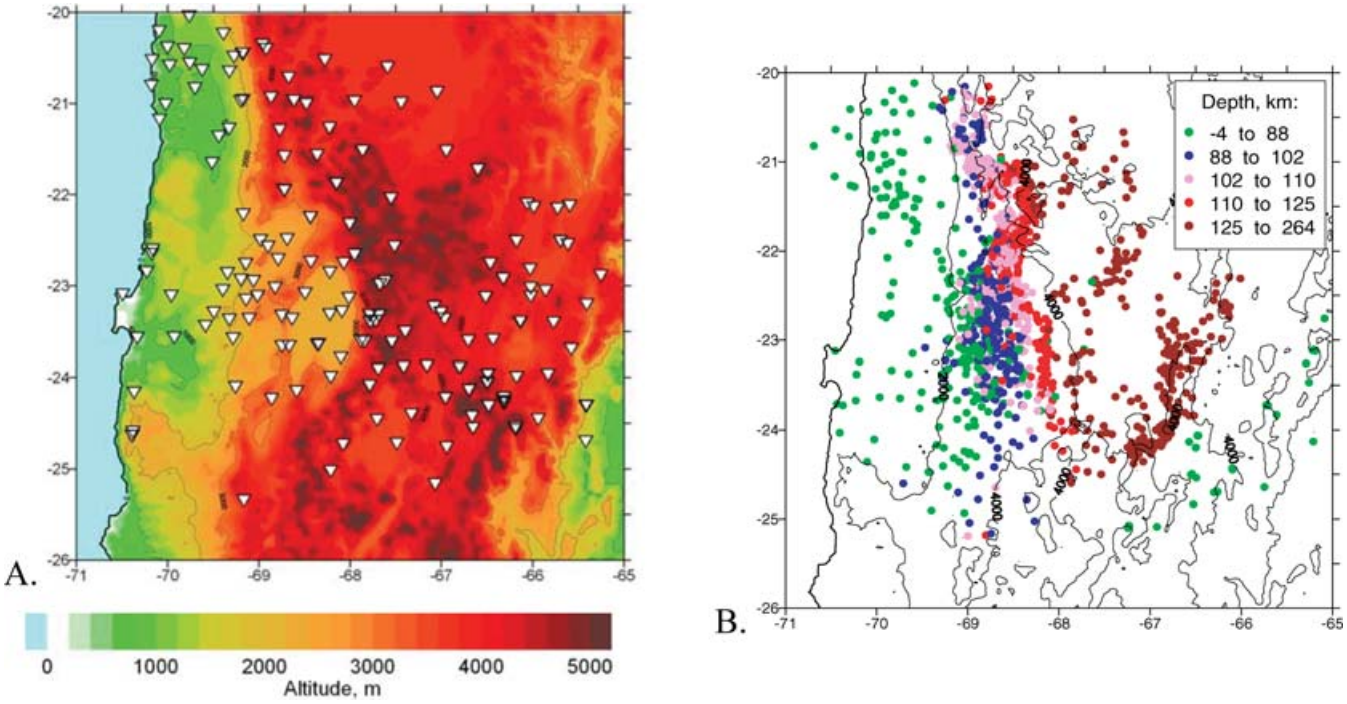

Figure 2. Initial data distribution. (a) Position of all stations used in this study. Contour lines show relief in the study area; (b) Seismic events used in the tomographic inversion at different depth intervals shown by different colours dots. Relief contour lines at 2000 and 4000 m are shown.

Table 1. '1-D-Minimal' starting model (Schurr 2001).

Z, km	*Vp*, km s^{-1}	*Vs*, km s^{-1}	*Vp/Vs*
−10	5.8	3.31	1.752
60	6.21	3.62	1.715
60	7.91	4.42	1.789
80	7.99	4.45	1.795
100	8.17	4.45	1.835
120	8.41	4.87	1.726
160	8.75	4.87	1.796
220	8.85	4.82	1.836
500	9	4.9	1.836

Although the previous tomographic models show many interesting features, we believe that inversion of the seismic data in Central Andes should be revised. There are several reasons to do that. First of all, the basic assumptions of the previously used algorithm may not work correctly in the complex structure of the Central Andes. The starting 1-D model, which fits best to the observed traveltimes (Table 1) averages slab and mantle wedge and thus strongly stimulates smearing of high seismic velocities from the slab towards the wedge in the final 3-D model. As the result, the absolute velocities in the wedge are generally higher than could be expected from petrophysical point of view (see Section 5.1 below). More over, seismic velocities in mantle wedge in places appear to be higher than in the cold slab, which is difficult to explain (see Fig. C1 in Schurr 2001). Secondly the inversion algorithm used in the previous studies (Graeber & Asch 1999; Schurr 2001; Schurr *et al.* 2003) employs very simple, even parametrization of the modelling domain. Thus it neither takes into account strongly uneven distribution of the rays, nor attempts to separate seismic anomalies in the physically distinct parts of the model, that is, in the crust, mantle wedge and slab. We believe that tomographic inversion in the extremely heterogeneous region like Central Andes, which includes cold slab and hot (and wet) mantle wedge possibly containing partial melts, requires special inversion approach. The inversion technique we employ in this paper uses 3-D starting model including interfaces, involves accurate shooting ray tracer, employs advanced algorithm of source localization (including double-difference algorithm of relocation), and uses non-uniform parametrization with double points at the interfaces. We also investigate effect of different 1-D starting models on inversion results.

2 INVERSION STRATEGY

The tomography with natural sources is always a poorly set problem (Nolet 1987). In fact, the input information contains only the exact coordinates of seismic stations and arrival times of the rays from unknown sources. In the output of the tomographic inversion a set parameters is obtained: 3-D velocity field, position and origin times of sources and station corrections. In case the expected velocities are close to 1-D model (up to 3 per cent of relative anomalies), a linear approach starting from 1-D velocity model can provide a fairly stable solution (Nolet 1987). In the Andes such strong velocity features as high-velocity subducted slab and low-velocity asthenosphere upwelling in the mantle wedge (e.g. Schmidt & Poli 1998) may produce strong velocity anomalies with the amplitude of above 10 per cent. In this case the actual ray paths are significantly different from the ray paths computed in the 1-D model, and even iterative quasi-linear approaches do not necessarily lead to the true solution. Due to the principal non-uniqueness of the inverse problem, it is important to define a realistic starting model based on an *a priori* information. The idea of the 3-D starting model has been successfully realized in (Nakajima *et al.* 2001) for investigation of the mantle wedge in Japan. In our work the tomographic inversion starts with the 3-D reference model, which is constrained from available *a priori* information. A detailed description of this reference model is given in the Section 3.

Table 2. '1-D-Non-Slab' starting model (our work).

Z, km	*Vp*, km s^{-1}	*Vs*, km s^{-1}	*Vp/Vs*
20	5.8	3.31	1.752
60	6.7	3.82	1.754
60	8.016	4.529	1.770
70	7.999	4.501	1.777
80	7.98	4.471	1.785
90	7.959	4.439	1.793
100	7.937	4.404	1.802
150	8.079	4.451	1.815
200	8.222	4.504	1.825
250	8.354	4.552	1.835

In our model, after defining the starting model, the sources are relocated on the basis of the arrival times of *P* and *S* rays (Section 4.2) with the use of the ray tracer algorithm designed for complex 3-D velocity medium (Section 4.1). After that the sources are relocated with the use of the double-difference algorithm (Section 4.3). The obtained residual times are used as input to the block of the tomographic inversion (Sections 4.2 and 4.3). The matrix inversion implies the simultaneous reconstruction of *P* and *S* velocity parameters, source parameters and *P*, *S* station corrections. The obtained *P* and *S* velocity anomalies are superimposed with the starting velocity model and are used as basic model for the next iteration, which starts from the step of the source location. When a contribution of the next step becomes negligible, the iterative procedure stops.

3 1-D AND 3-D INITIAL MODELS

In the previous work performed for the same data set by Schurr *et al.* (1999) and Schurr (2001) the inversion started from determination of optimal 1-D velocity model. It was obtained using the algorithm developed by Kissling *et al.* (1994). In this method the sources are relocated simultaneously with determination of 1-D model that provides the best fit with the observed arrival times. The values of *P* and *S* velocities at different depths according to this model (hereafter called '1-D-Minimal model') are given in Table 1. Although this model fits well with the observed data, its petrophysical interpretation is problematic. In particular, it is hard to explain the *S*-velocity jump from 4.45 to 4.87 km s^{-1} at the depth of 120 km and very low ratio $Vp/Vs = 1.72$ between 120 and 160 km of depth. The values of *P* velocity in all ranges of depth seem to be higher than expected within the mantle wedge. Apparently, the faster velocities are related to the rays travelling in the high-velocity slab. As the result, the tomographic inversion starting from 1-D-Minimal model (Schurr *et al.* 1999) and our results described in Section 5), provide unrealistic values of absolute velocities, but formally fairly good fit to the data (0.217 s rms misfit).

An alternative approach is to define the 1-D starting model from independent *a priori* information ignoring existence of the slab. We composed such model (hereafter called '1-D-No-Slab' model) based on the information about average depth distribution of temperature, density, pressure, etc. in the mantle wedge using the relationships from (Sobolev & Babeyko 1994; Sobolev *et al.* 1996, 1997) (Table 2, see also below). The 3-D tomographic inversion (Section 5), based on the '1-D-No-Slab' starting model provide reasonable values of absolute velocities in the mantle wedge and also image the slab. However, the fit to the data in this case (0.233 s) is significantly worse than in the 1-D-Minimal model (0.217 s). Apparently, the problem of the inversion with the '1-D-No-Slab' starting model is that the starting model, which does not take into account presence of the cold high-velocity slab appears to be too far from reality to allow optimal solution.

To obtain realistic velocity model and best data fit in a complex crust–slab–asthenosphere system as in Central Andes, a 3-D velocity model constrained from *a priori* information is proposed as a starting (reference) model. This model, hereafter called 'CWS' model (crust, wedge, slab) (Fig. 3), consists of three separate zones of different velocity structures. These zones are:

(1) **Continental crust**, with Moho topography defined from receiver-function analysis (Yuan *et al.* 2000, 2002). Averaged 1-D crustal velocities estimated from wide-angle reflections (Wigger *et al.* 1994) are presented in Table 3. In this model we assume that most of the crust has felsic or intermediate composition (e.g. Yuan *et al.* 2002) and use the modelling technique by Sobolev & Babeyko (1994) to calculate expected seismic velocities in such a crust;

(2) **Mantle wedge**, located between the crust and the slab, with the 1-D velocity distribution (Table 4) defined from petrophysical constrains. To do so we use average peridotite composition, temperature distribution for 100-km-thick lithosphere and petrophysical modelling techniques to calculate seismic velocities from given chemical composition, pressure and temperature (Sobolev & Babeyko 1994; Sobolev *et al.* 1996, 1997). We note that the above techniques use realistic mineral compositions of rocks changing with pressure and temperature and take into account both contribution of anharmonic and anelastic effects on seismic velocities;

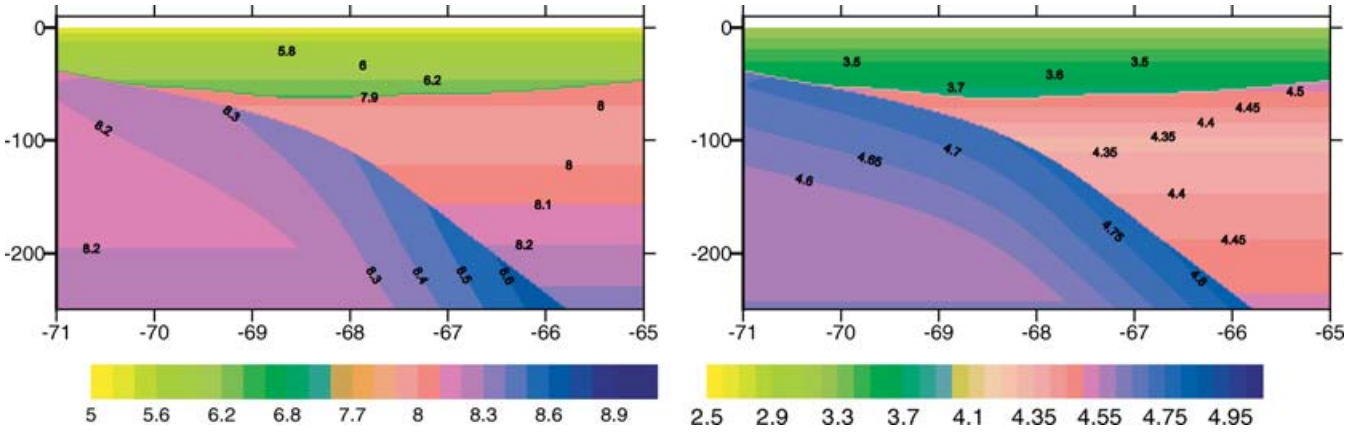

Figure 3. Vertical sections of *P* (left) and *S* (right) initial velocity distribution in the '3-D-Complex model' at the latitude of 23.4°.

Table 3. Basic 1-D model in zone 1 (crust) of the 3-D-Complex model.

Z, km	*Vp*, km s^{-1}	*Vs*, km s^{-1}	*Vp/Vs*
−10	5	3.1	1.613
20	5.8	3.41	1.70
60	6.7	3.76	1.70

Table 4. Basic 1-D model in zone 2 (mantle wedge) of the 3-D-Complex model.

Z, km	*Vp*, km s^{-1}	*Vs*, km s^{-1}	*Vp/Vs*
60	8.016	4.529	1.769
70	7.999	4.501	1.777
80	7.98	4.471	1.784
90	7.959	4.439	1.792
100	7.937	4.404	1.802
150	8.079	4.451	1.815
200	8.222	4.504	1.825
250	8.354	4.552	1.835
310	8.665	4.696	1.845

(3) **Slab**, with the upper boundary defined from the seismicity in the Wadati-Benioff zone. The preliminary location of deep sources was computed in the '1-D-No-slab' model after eliminating the rays travelling in the slab. The surface of the slab was constructed manually as upper envelope of the deep earthquakes as shown in Fig. 4. Initial velocity distribution in the slab is defined as superposition of basic velocity, $V^0_{\rm slab}(z)$ defined in the Table 5 and the additional term that simulates expected standard velocity contrast between slab and wedge, which depends on distance from the surface of the slab:

$$V_{\rm slab}(x, y, z) = V^0_{\rm slab}(z) + dV(dS, z), \quad (1)$$

where dS is distance from the current point to the surface of the slab. We set $dV(ds, z)$ as:

$$dV(dS, z) = \begin{cases} (dV_{\max}(z)/dS_{\max})(dS_{\max} - dS), & \text{when } dS < dS_{\max} \\ 0 & \text{when } dS > dS_{\max} \end{cases}, \quad (2)$$

$dV_{\max}$ is velocity contrast between slab and mantle wedge, $dS_{\max}$ is thickness of the slab. In the actual work we used the following values of the parameters: $dS_{\max} = 100$ km, $dV_{\max}$ (50 km) = 4 per cent, $dV_{\max}$ (250 km) = 5 per cent. In other depths the values of the velocity contrast were linearly interpolated.

A special attention in setting up of the starting model was paid to the algorithm of smooth interpolation of functions in different dimensions: 1-D (for interpolation of 1-D velocity distribution), 2-D (for interpolation of surfaces between zones) and 3-D (for smooth presentation of the obtained field of velocity anomalies $dV(x, y, z)$). We developed an algorithm of 1-D smoothing by flattening of edges of a linearly interpolated function with polynomials of third order. This algorithm was expanded to 2-D and 3-D cases.

Table 5. Basic 1-D model in zone 3 (slab) of the 3-D-Complex model.

Z, km	*Vp*, km s^{-1}	*Vs*, km s^{-1}	*Vp/Vs*
40	7.8498	4.5068	1.741
50	7.9382	4.5448	1.746
100	8.0360	4.5619	1.761
150	8.1244	4.5771	1.775
200	8.2070	4.5894	1.788
250	8.2878	4.6018	1.800

4 ALGORITHM OF TOMOGRAPHIC INVERSION AND SOURCE LOCATION

4.1 Source location

In the problem of non-linear tomography most of the computing time is consumed by two-points ray tracing in 3-D space. To realize non-linear tomographic inversion in reasonable computing time, the tracing algorithm must be sufficiently fast. There are rather fast and stable approximate methods (e.g. bending method by Virieux *et al.* 1988 or by Um & Thurber 1987) that allow significant economy of computer resources. Approximate methods are good for smooth velocity models, but in media with non-horizontal boundaries and strong velocity anomalies they can cause significant errors. To do ray tracing we use the shooting method (Cerveny *et al.* 1977), which determine the ray between two fixed points after several trial 'shots'. Details of our ray-tracing algorithm are given in the Appendix 1.

The problem of localization of sources is one of the most important in seismology. The standard routines in most cases employ the classical approaches developed a long time ago (e.g. Crosson 1976), which are based on rather simplified velocity models and ray tracing in 1-D velocity models. During the last decades, methods based on approximate ray tracers in 3-D media (Virieux *et al.* 1988) are actively developed. However, source location with the use of exact methods of 3-D ray tracing is not widely applied in practice due to large computing time required.

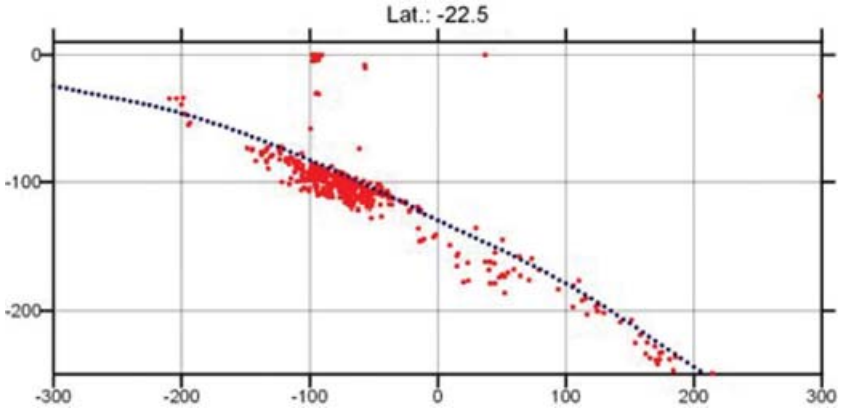

Figure 4. Example of the manual construction of the upper surface of the slab as envelope of seismicity in the Benioff zone. Position of sources shown by dots is computed in the 1-D-Petrophysical model.

In this work the location of sources is performed through three successive steps:

(1) absolute location of sources,
(2) relocation of source parameters by double-difference algorithm and
(3) simultaneous correction of the sources parameters and the velocity parameters at the step of tomographic inversion (Section 4.2).

The absolute location of a source is realized by searching a point in which the best correspondence with the observed traveltimes is achieved in the current fixed 3-D *Vp*-*Vs* model. The residual times dt_{ij} are computed iteratively. At Nth iteration,

$$dt_{ij}^{N} = dt_{ij}^{N-1} - \left\{ \sum_{j=1}^{M_i^{N-1}} A_{PS}\, dt_{ij}^{N-1} \right\} \Big/ M_i^{N-1}, \tag{3}$$

where M_i^{N-1} is number of 'good' observations (i.e. observations with residuals less than a predefined value; $dt^{\max}$) and A_{PS} is a weight function depending on P or S phase. It is assumed that P phases are more valuable for source location than S phases; hence they are given twice greater weights for determination of the origin time.

At the first iteration,

$$dt_{ij}^{0} = t_{ij}^{\text{obs}} - t_{ij}^{\text{ref}} \quad \text{and} \quad M_i^{0} = M_i, \tag{4}$$

where t_{ij}^{obs} is the observed and t_{ij}^{ref} the reference traveltime between the ith source and the jth station. M_i is the total number of recorded phases for the ith source. The maximal residual among all phases is identified and if it is greater than a predefined value $dt^{\max}$ (0.7 s for P waves and 1 s for S waves), it is rejected from the source location. For example, when the location of sources was performed in a 1-D model ('Minimum' or 'No-Slab'), the rays travelling in the slab and having big residuals were rejected and were not used for source location. At the same time, at the step of tomographic inversion, a limit of data rejection was higher: 2 s, for P rays and 3 s for S rays. Consequently, the slab travelling rays where included in inversion and used to define 3-D velocity model.

To find the source coordinates and the origin time, it is necessary to define the probability function of a source existing in any point of the study area. Here we propose two criteria. The primary criterion is the number of 'good' observations meaning those observations with residuals less than a predefined value $dt^{\max}$. The secondary criterion is the value of the goal function defined as:

$$G = \sqrt{\sum_{j=1}^{M^{\text{good}}} dt_j^2 \Big/ M^{\text{good}}}, \tag{5}$$

where dt_{ij} is the residual measured for i source at the j station and M^{good} is the number of good observations. The preliminary position of a source is determined by searching in a regular grid constructed around the preliminary location of source. The lateral size of the grid has been 30 km with nodes spread in 5 km intervals. Out of those nodes with maximum numbers of 'good' residuals we select one where the goal function has the minimum value. From the selected node, components of the direction vector (dx, dy, dz) along which the goal function decreases more rapidly are determined by solving the following system of linear equations:

$$P_i^x\, dx + P_i^y\, dy + P_i^z\, dz + dt^0 = dt_i \quad i = 1 \ldots M^{\text{good}}, \tag{6}$$

where P_i is the slowness vector of the ith ray in the source point. This system is solved by the least-square method. If the number of 'good' observations in the next point is greater than in the previous point, or when it remains unchanged whereas the value of the goal function becomes smaller, we move to the next point. Otherwise, the midpoint of the direction vector is taken as the next point. The procedure continues until a point is reached from which the minimal step displacement in any direction leads to a greater value of the goal function.

Relative locations of events in a cluster are adjusted using the double-difference method (Waldhauser & Ellsworth 2000). It is based on the assumption that the residuals from two sources located close to one another and recorded at one station should have similar value. The algorithm finds the coordinates and origin time corrections to minimize all possible double differences. We construct a linear system of equations for all combinations of couples of sources (e.g. with numbers k and m) located less than a distance $dS^{\max}$ apart from one another (15 km in our case) and having a common observation i (the same station and the same P or S phase):

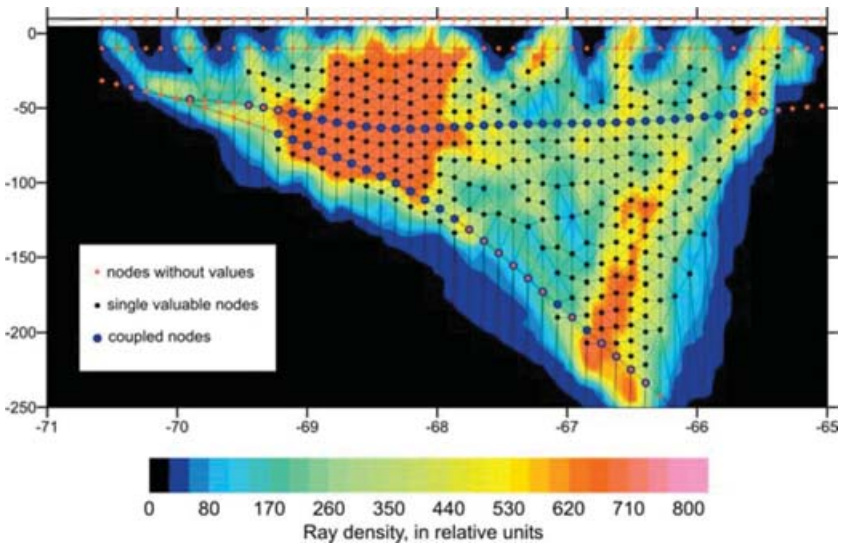

Figure 5. Example of the parametrization grid construction according to the ray density, vertical section at 23° of latitude.

$$(P_x)_{ik}\,dx_k + (P_y)_{ik}\,dy_k + (P_x)_{ik}\,dy_k + dt_k^0 - (P_x)_{im}\,dx_m - (P_y)_{im}\,dy_m - (P_x)_{im}\,dy_m - dt_m^0 = dt_{ik}^{\mathrm{obs}} - dt_{im}^{\mathrm{obs}}. \quad (7)$$

As the result, we obtain a system of linear equations with number of column equal to number of sources multiplied by four. Every row contains eight non-zero elements. For 1500 sources, number of equations is about one million. This system can be inverted using iterative LSQR method (Van der Sluis & van der Vorst 1987). Following the inversion, the source parameters are updated and the procedure is repeated four to five times until it converges. A typical average shift of the sources after the double-difference relocation in our inversions was about 1.5 km. After this step the sources in the slab were localized in a slightly thinner layer.

4.2 Parametrization and inversion for *Vp* and *Vs*

Parametrization of the velocity field for the tomographic inversion is performed on the basis of the node parametrization method developed in our previous works (e.g. Koulakov 1998; Koulakov *et al.* 2002). A certain amount of nodes is distributed inside the study volume according to the ray density, so that approximately equal summary length of rays was observed around each node. The nodes are joined together into a tetrahedral grid. Inside every tetrahedron, velocity is linearly approximated. The nodes are distributed in some sets of parallel planes. In every plane, the nodes lie on some parallel lines. In the actual work we distribute the nodes on vertical planes orientated across the subduction zone. The interfaces dividing different zones are parametrized with double-sided nodes, which allow sharp contrast of the velocities at different sides of the interface and thus are effective against smearing of the velocity anomalies. Introduction of the interfaces and their parametrization have already been used in few tomographic works (e.g. Funck *et al.* 2000). An example of node distribution at one plane is shown in Fig. 5. In this work we have used about 6000 valuable nodes for the *P* model and about 4000 nodes for *S* model.

The first derivative matrix A which reflects the effect of velocity variations at the ith node on the traveltime of the jth ray is computed by integration along the ray path γ as:

$$A_{ij} = \int_{\gamma} \Delta g_j(\gamma)\,dS \Big/ \Delta\sigma_j, \quad (8)$$

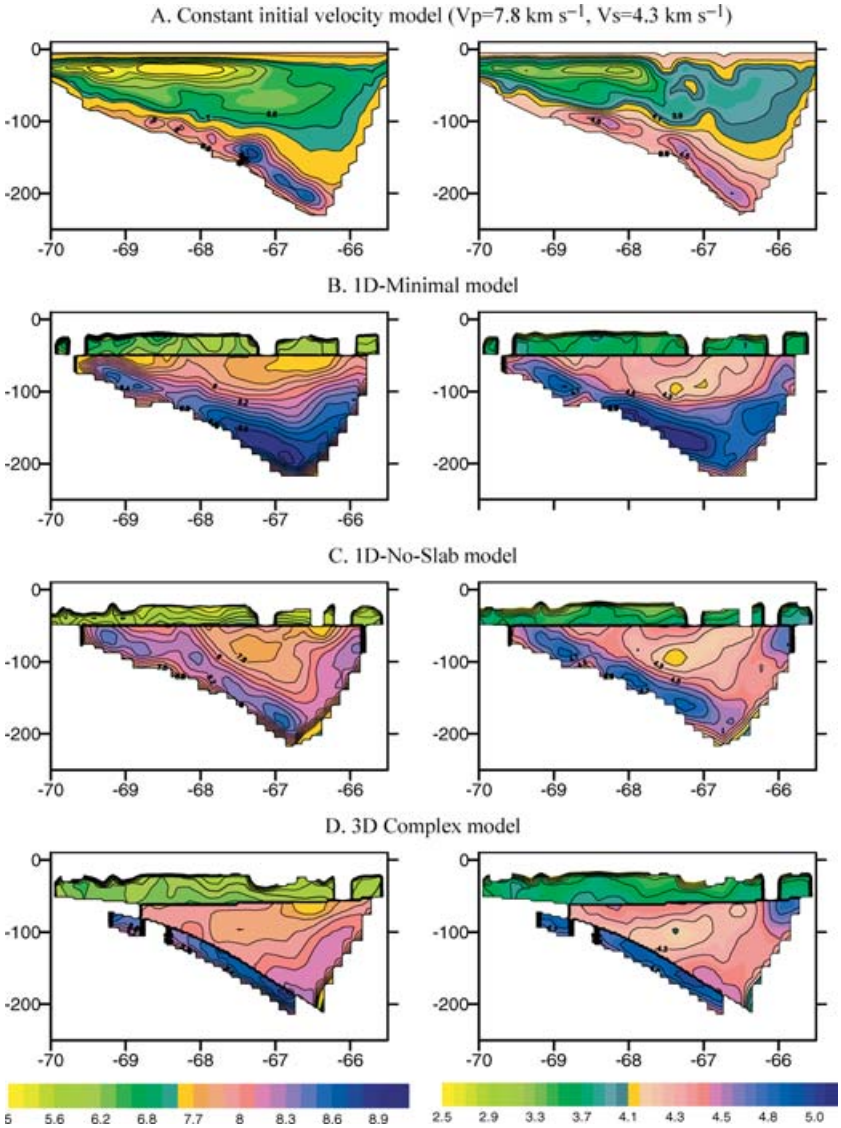

Figure 6. Result of inversion starting with different initial velocity models after five iteration steps, absolute *P* (left column) and *S* (right column) velocities. Vertical section corresponds to the latitude of 23.5°.

where Δg_j is a slowness perturbation at the current point of the ray related to unit slowness anomaly $\Delta\sigma_j$ at the jth node. Only the influence of the four vertices of the tetrahedron in which the point is located is taken as non-zero. Together with the elements responsible for the unknown P and S velocity anomalies, the matrix includes the elements for corrections of source parameters (four for each source) and station corrections. Smoothing of the resulting velocity anomalies is controlled by an additional matrix block. Each line in this block contains two non-zero elements with opposite signs which correspond to neighbouring nodes. Increasing weights of these elements has a smoothing effect upon the resulting anomalies.

As the result, we get nine controlling coefficients responsible for different sorts of unknown parameters: W1 and W2 regulate 3-D P and S velocity anomalies; W3 and W4 control the P and S station corrections. W5, W6 and W7 are responsible for horizontal, vertical shift of sources and for the origin time; W8 and W9 regulate smoothing of P and S velocity fields. Determination of all the coefficients in the matrix is a crucial and delicate task. Pavlis & Booker (1980) suggest a way to formalize the process using analytical methods. However, in our case, determination of weights for principally different sorts of parameters (e.g. velocity, time corrections and source shift) using these schemes was not successful. Probably there are too many factors that can influence these coefficients, such as the amount of data, the number of free parameters, noise level, etc. Therefore, we conclude that the values of the coefficients should be defined separately in each specific case based on the expected amplitudes of the sought parameters and synthetic tests.

The resulting matrix is inverted using the LSQR method (Paige & Saunders 1982; Van der Sluis & van der Vorst 1987). The number of LSQR iterations providing a satisfactory convergence in our case was 50.

As the result of the matrix inversion we obtain the values of velocity anomalies in the irregular grid. Before moving to the next iteration, the velocity field is computed in a regular grid and smoothed. The obtained station corrections are subtracted from the observed traveltimes. The next iteration starts from the step of absolute source location in new 3-D velocity model:

$$V^{\text{iter}}(x, y, z) = V_{\text{start}}(x, y, z) + dv^{\text{iter}}(x, y, z),$$

where $V_{\text{start}}(x, y, z)$ is the starting velocity model, which stays without changes in all iteration; $dv^{\text{iter}}(x, y, z)$ is a function of velocity anomalies, corrected at each iteration. When the change of $dv^{\text{iter}}(x, y, z)$ at a next iteration is not significant, the iterative process stops. In our case five iterations were enough to get a sufficient convergence.

4.3 Inversion for *Vp* and *Vp/Vs* ratio

Vp/Vs, or Poisson ratio is an important parameter which characterizes lithology and petrophysical state of the rocks. In many recent tomographic studies the inversion is performed for P-velocity anomalies together with variation of *Vp/Vs* ratio (e.g. Thurber 1993; Hauksson & Haase 1997; Graeber & Asch 1999; Schurr 2001). In most of these works perturbation of the *Vp/Vs* ratio is determined from analysis of S–P differential time variation with respect to a reference model. This approach assumes small difference between P and S ray paths, and the elements of Frechet matrix for *Vp/Vs* parameter are computed by integration along P rays. However, this assumption is too rough in areas with strong velocity contrasts where P and S ray paths can differ significantly. In this work we propose another algorithm of simultaneous inversion for *Vp* and *Vp/Vs* variations. Let us denote *Vp/Vs* parameter as X. If we assume that P and S traveltimes are functions of *Vp* and X, full differentiation results in:

$$dt_p = \frac{\partial t_p}{\partial V_p}\, dV_p$$

$$dt_s = \frac{1}{X}\frac{\partial t_s}{\partial V_s}\, dV_p - \frac{V_p}{X^2}\frac{\partial t_s}{\partial V_s}\, dX,$$

where $\frac{\partial t_p}{\partial V_p}$ and $\frac{\partial t_s}{\partial V_s}$ are the elements of the Frechet matrix, the same as used in tomography for P and S velocity anomalies (Section 4.2). They are computed by integration along corresponding P and S rays. It is important that in this case P-velocity anomalies are affected by both P and S residuals, while the X anomalies are only related to the S residuals. Furthermore, each line of the matrix contains four additional elements responsible for the source parameters and one element of the station correction. Besides the changes in the matrix structure, a strategy of full iterative inversion is the same as the main tomographic inversion for P and S velocities described above.

4.4 Inversion for *Qp*

In addition to P- and S-wave traveltimes, seismological data set for Central Andes collected by the SFB 267 seismological team also contains data related to the P-wave attenuation (so called

Table 6. values of summary data misfit (in seconds) for different starting models during five iterations.

	Iterations:	1	2	3	4	5
'Constant' starting model	total:	0.668	0.481	0.447	0.436	0.432
	P-residuals	0.564	0.426	0.404	0.396	0.393
	S-residuals	0.831	0.573	0.520	0.504	0.498
'1-D-Minimal' starting model	total:	0.346	0.246	0.228	0.221	0.217
	P-residuals	0.301	0.205	0.189	0.184	0.180
	S-residuals	0.424	0.311	0.290	0.280	0.274
'1-D-No-Slab' starting model	total:	0.388	0.263	0.244	0.236	0.233
	P-residuals	0.356	0.227	0.208	0.202	0.199
	S-residuals	0.450	0.323	0.302	0.292	0.287
'3-D-Complex' starting model with slab,	total:	0.359	0.247	0.229	0.220	0.216
mantle wedge and crust constrained	*P*-residuals	0.325	0.207	0.191	0.184	0.180
from petrophysics	*S*-residuals	0.421	0.310	0.288	0.278	0.272

t^* times) (Schurr 2001; Haberland & Rietbrock 2001; Haberland *et al.* 2003). The data set pre-processed by Schurr (2001), (see also Schurr *et al.* 2003) contains about 25 000 values of t^* recorded from ∼1500 events, generally the same as used for velocity tomography. This data set has been already used for tomographic inversion resulting in 3-D distribution of *Qp* parameter (Schurr *et al.* 2003). In our study we repeat the inversion of t^* for *Qp* using the positions of sources and ray paths computed after five iterations of the velocity tomographic inversion. The method of parametrization, matrix calculation and inversion that we used in the attenuation tomography was similar to the method of velocity tomography.

5 RESULTS

5.1 Inversions with different starting models

Here we present the results of full tomographic inversion starting from different velocity models. The absolute *P* and *S* velocities at the section −23.5° obtained after five iterations of inversion are shown in Fig. 6.

The values of data misfit during five iterations of inversion for different starting models are given in Table 6. Standard deviations (rms) of *P* and *S* residuals separately and of summary data set

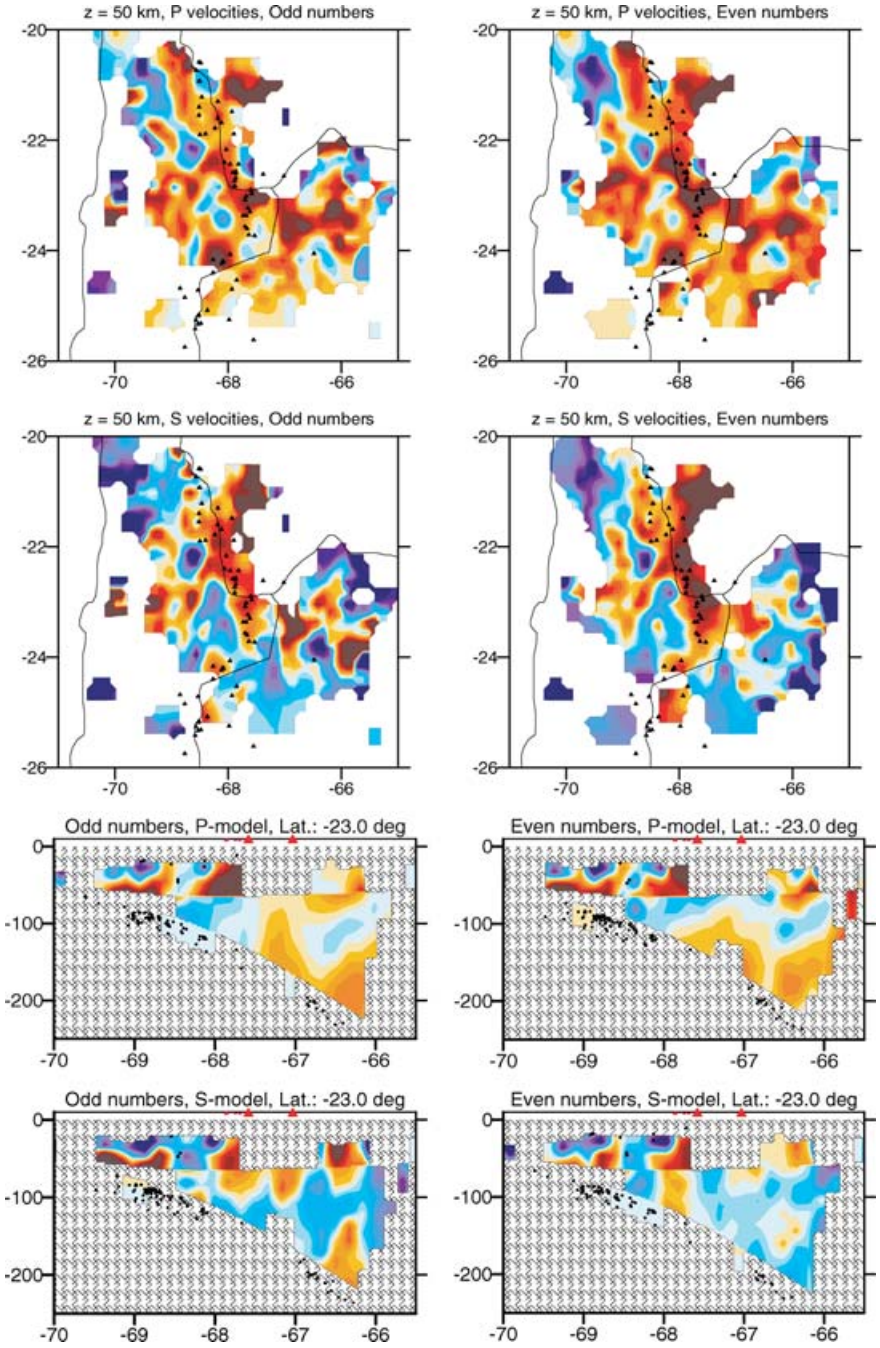

Figure 7. Test with independent reconstruction of two data subsets: with odd (left column) and even (right column) numbers of events. Two upper rows show horizontal sections at 50 km depth of the resulting *P* and *S* models. Two lower rows are the vertical sections of the same models at the latitude of −23°. Positions of the events along the profile used in each subset are shown by black dots. Triangles show position of recent volcanoes (less than 2 Ma of age).

correspond to the step just after the absolute source location at each iterative cycle. The values of rms at the first iteration reflect the data fit provided by the starting model.

The first model (Fig. 6a) was derived from the constant initial velocity model with 7.8 km s^{-1} of *P* velocity and 4.3 km s^{-1} of *S* velocity. The aim of this trial was to check capacity of the algorithm to get reasonable features without use of any *a priori* information. As the result, we can distinguish the high-velocity slab with the geometry close to the expected position. The low-velocity crust is fairly well constrained in the western part of the study volume, though in the eastern part it is not detectable. The values of absolute velocities seem to be far from the real values.

The results of inversion derived from 1-D-Minimal and 1-D-No-Slab models defined in the Section 3 are presented in the Figs 6(b) and (c). The resulting absolute velocities in the '1-D Minimal' model seem to be unreasonable. Indeed, the value of *P* velocity equal to 8.7 km s^{-1} in the mantle wedge at the depth of 150 km corresponds to the temperature less than 200°C (Sobolev *et al.* 1996), which could never be expected in the mantle. At the same time, this model provides significantly better variance reduction than the 'No-Slab' model, which is derived from the petrophysical information.

The CWS model (Fig. 6d), constrained from *a priori* information, provides the same variance reduction as 1-D-Minimal model and reasonable resulting velocities. The tomographic inversion starting from the 3-D CWS model is the main result of this study and it will be presented in detail later.

Inversion with different initial models clearly demonstrates the non-uniqueness of the inverse problem with natural sources. Quite different velocity models can be equal in sense of data fit. Only utilization of *a priori* information, such as distribution of earthquakes and other geophysical (especially other seismic) observations as well as mineral-physics constraints, can reduce ambiguity of the inversion result.

5.2 Resolution tests

To explore the influence of random error in the data, we have made the test in which the total amount of data is subdivided into two equal groups by an arbitrary way (in our case, corresponding to the earthquakes with odd and even numbers). All processing procedures are realized independently for these two groups of data. Differences in the final models reflect the role of the random factor in the data. Also, comparison with the results of inversion of the entire data shows how halving of the total number of data affects the model resolution. In our case, the results of this test (Fig. 7) provide generally high resemblance of all images that is an indicator of the high quality of the initial data and stability of the inversion. In particular, in the forearc even small patterns (up to 10 km size) are present in both odd- and even-number models. In the backarc the correlation is less obvious; nevertheless the main patterns of more than 30–40 km dimension are reconstructed reliably. It is important that despite significantly larger noise level in *S* data, correlation of images in *S* model is not poorer than in *P* model. This is due to the generally higher sensitivity of *S* wave to anomalies in the crust and the mantle, that largely compensates the error related to higher noise level. Comparison of the images obtained in this test can help to evaluate real resolution of the resulting model. In our opinion it is a more correct way to assess model resolution than the typically used plotting of resolution matrix or checkerboard tests, since it takes into account real noise distribution, which can vary in different parts of the study area.

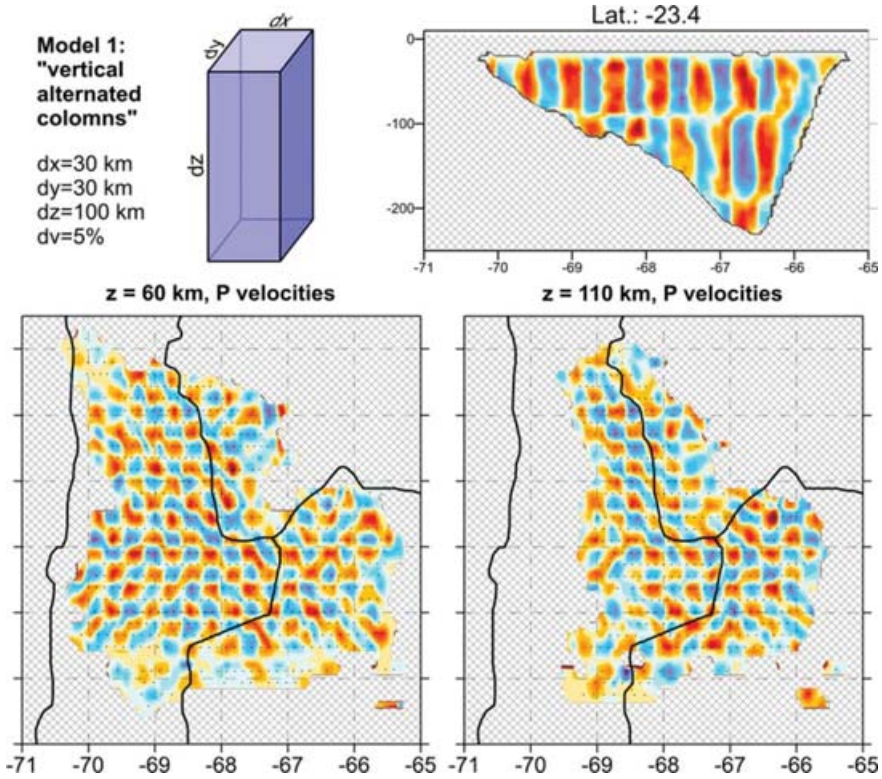

Figure 8. Reconstruction of the synthetic anomalies consisting of alternated positive and negative blocks with the parameters shown in the upper-left figure. Results of reconstruction are presented at one vertical section (upper-right) and two horizontal sections. Parametrization nodes at the horizontal sections are shown with black dots.

However, following the established tradition of presentation of the tomographic studies, we present here also the result of the checkerboard test, which gives an idea about theoretical capacity of the inversion algorithm to reconstruct anomalies of fixed size. The input residuals for the inversion are computed along the real rays (e.g. *P* waves) traced through synthetic anomalies. Reconstruction of the anomalies is performed only at the step of tomographic inversion without relocation of sources. We considered different sorts of synthetic models (e.g. single positive or negative anomaly of different sizes, different groups of blocks, etc). Here we present one example of alternated positive and negative blocks. Parameters of the blocks and results of inversion on both vertical and horizontal sections are shown in Fig. 8. This test shows that the anomalies with the horizontal size of more than 30 km are reliably reconstructed in most parts of the study area. However, under Altiplano plateau this test shows lower resolution due to the lack of the data.

Another test shown in Fig. 9 seems to be more realistic than checkerboard test since it takes into account shape of the resulting anomalies, real data noise and is performed using the full iterative inversion procedure. The shapes of the synthetic anomalies were taken as the approximate contouring of the velocity patterns at the resulting images in Fig. 10 (bold black lines). The synthetic traveltimes were computed by the shooting ray tracing, same as used in the main algorithm. Furthermore, the random noise with the standard deviation similar to the expected in the real data (0.2 s for *P* waves and 0.4 for *S* rays) was added. The reconstruction of the anomalies has been performed during full iterative procedure, which includes source relocation. Weighting parameters for the inversion were the same as in the real-data inversion.

The test, which results are shown in upper row of Fig. 9, is aimed to investigate the reliability of the inversion results at 21°S. The initial velocity model consisted of four alternated positive and negative anomalies in the crust. The anomalies were centred at 21°S and were 100 km long perpendicular to the section at 21°S. The Amplitude of the anomalies was ±8 per cent with respect to the reference velocity model in the crust. The results of reconstruction of *P* and *S* velocity anomalies show fairly good horizontal resolution and slightly poorer vertical resolution in the crust. This fact can be explained by domination of quasi-vertical rays from sources located under the Moho. Note, however, that no much smearing of the crustal anomalies into the mantle is observed, especially in the model part west of −68°.

Another test, presented in the lower row of Fig. 9, was aimed in explore the resolution at 23°S. Two anomalies, ±8 per cent, one under another, were defined in the crust, and one negative anomaly (−10 per cent) in the slab. In addition, a positive anomaly 5 per cent of amplitude was fixed in the mantle wedge. The result of inversion demonstrates good vertical resolution in the crust allowing to detect a transition between two quasi-horizontal anomalies. The anomaly in the slab, where most of sources are located, is also fairly well resolved, that was not obvious due to trade-off of velocity and source parameters in the inversion. The positive anomaly in the mantle wedge is reconstructed generally correctly. The artefacts in the crust above this anomaly are related to the dominant direction of the rays and should be taken into account when the real anomalies are considered.

5.3 Images of *Vp* and *Vs* variations

The best final model was selected among a number of solutions based on various 3-D CWS models with slightly different shape of the interface, velocity gradient in the crust, velocity contrast between the slab and mantle wedge. We tried also different values of weight parameters in the step of inversion to investigate their influence on the results. Determination of weights was based on expected values of the sought parameters and best fit with the input data. As a result, we got the model, which fits the data best and is consistent with the *a priori* information. The parameters of inversion are given in Table 7.

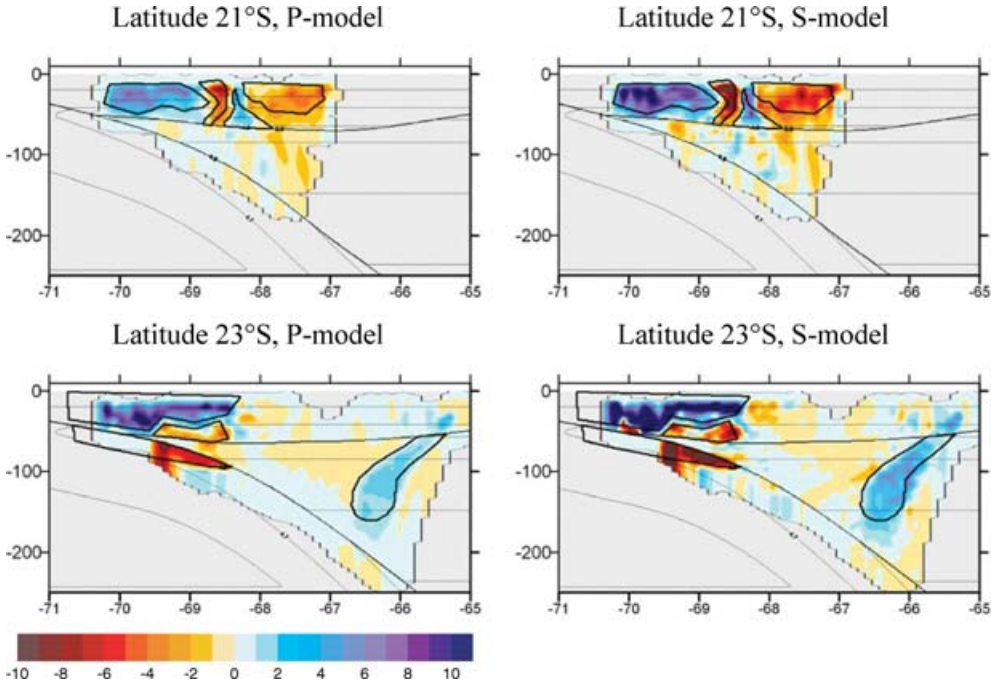

Figure 9. Synthetic test based on the shape of the anomalies obtained in the resulting model. Initial anomaly is contoured by bold line. Upper row: *P* and *S* anomalies reconstructions for the model defined at 21°S. Lower row: reconstruction for the model at 23°S.

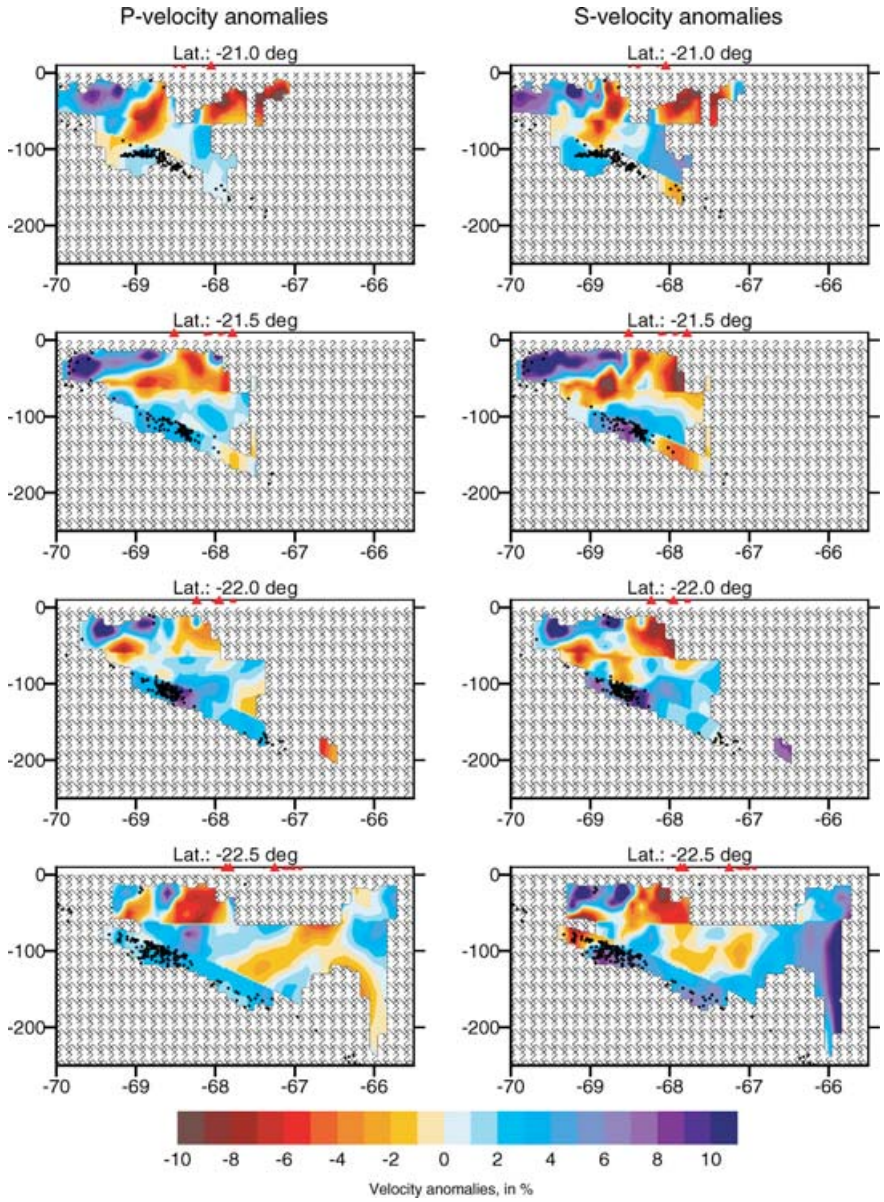

Figure 10. Vertical sections of the resulting *P* and *S* velocity anomalies derived with respect to '3-D-Complex' velocity model at different latitudes. Positions of relocated sources at the distance less that 30 km from the profiles are shown by black dots. Positions of recent volcanoes with the age of less than 2 Ma are indicated with red triangles.

Table 7. Parameters of inversion for the best model.

Number of iteration of general inversion	5
Number of iterations in LSQR inversion	50
Smoothing factor for *P*-model	0.5
Smoothing factor for *S*-model	1
Amplitude factor for *P*-model	1
Amplitude factor for *S*-model	1
P-station corrections weight	0.1
S-station corrections weight	0.1
Weight for horizontal source relocation	5
Weight for vertical source relocation	5
Weight for the origin time	1

In Fig. 10 we present eight vertical sections of relative *P* and *S* velocity anomalies with respect to the starting model. Blue colours mean positive velocity anomalies. Contour lines are in 1 per cent. The sections are given from north to south at every half degree. The relocated sources at distance of no more than 20 km from the sections are shown with black dots. The recent volcanoes (not older than 1 Ma) are shown with red triangles above the sections. Sizes of the triangles depend on the volcanoes volumes (de Silva & Francis 1991). Values of velocity anomalies are shown only if the distance to the nearest node of parametrization grid is no more than 30 km.

The horizontal sections of seismic *P* and *S* anomalies at the depths of 25, 50, 85 and 130 km corresponding to the middle and lower crust and uppermost mantle are presented in Fig. 11. In the mantle wedge and in the crust the anomalies are given with respect to the velocity values in the CWS starting model. In the slab the perturbations are shown with respect to the absolute velocities in the mantle wedge at the corresponding depth. The recent volcanoes are shown by black triangles. The most important feature in the middle crust image is very high values of *P* and *S* velocities (up to 10 per cent of anomalies) in the forearc. In the lower crust the structure under the forearc becomes more heterogeneous: beneath the Precordillera we

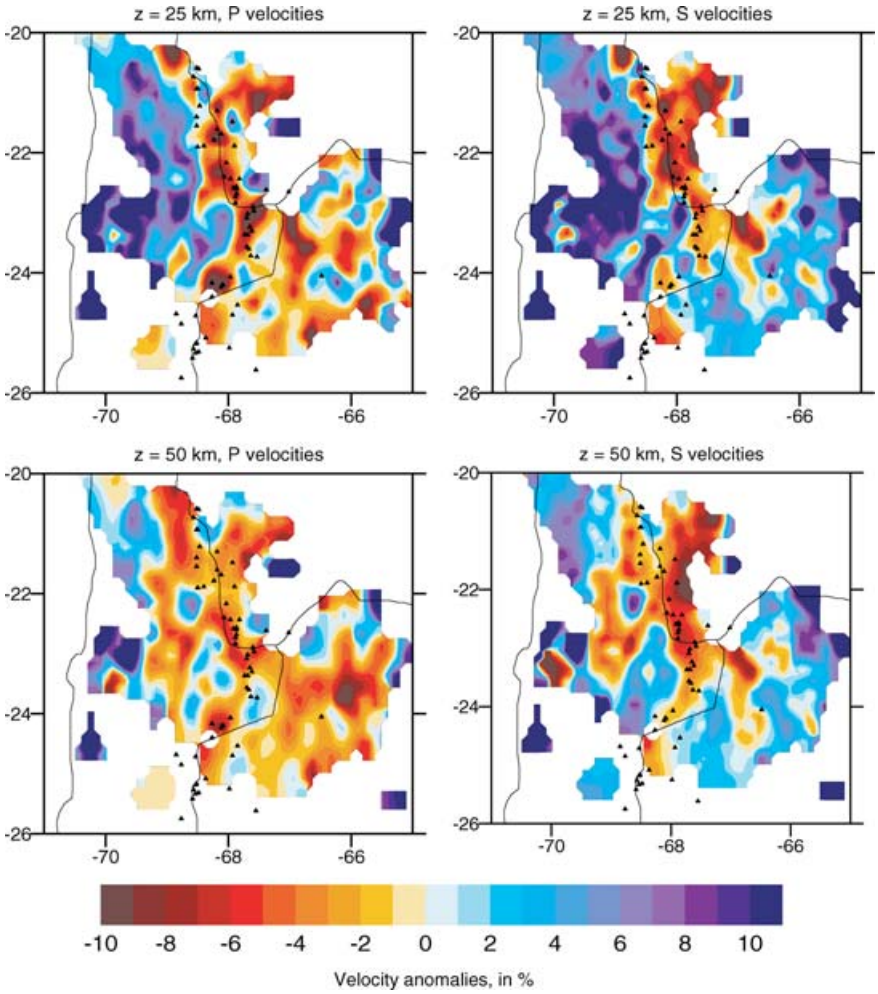

Figure 11. Horizontal sections of the resulting *P* and *S* velocity anomalies derived with respect to '3-D-Complex' velocity model at different depths. Positions of recent volcanoes with the age of less than 2 Ma are indicated with black triangles.

can observe a negative seismic anomaly, which fits well to the gravity residual field (Hackney, personal communication, 2005; Götze *et al.* 1994). Strong high-velocity anomaly with the centre at 68.2°W–23.5°S surrounded by low-velocity belts fits in both *P* and *S* models with the Salar de Atacama block. The present-day volcanic arc is associated with low velocities in the crust. In the backarc the crustal structure is significantly more complicated: alternated positive and negative anomalies indicate the mosaic structure of the crust.

5.4 Images of *Vp*/*Vs* ratio

Results of inversion for *Vp/Vs* parameter are given in Fig. 12. Here we show the anomalies with respect to the values of *Vp/Vs* in starting model (in absolute units). The area where the density of *S* rays is not sufficient is shaded, and reliability of the resulting anomalies there is lower. The criterion for definition of the well-resolved area for *Vp/Vs* ratio is more strict than that for presentation of *P* and *S* anomalies. The results of inversion for *Vp* and *Vp/Vs* are consistent with results of inversion for *Vp* and *Vs* (main results, Section 5.3). Comparison of the results of direct inversion for *Vp/Vs* shown in Fig. 13 with the *Vp/Vs* derived by subdivision of absolute velocities after five iterations of inversion for *Vp* and *Vs* (Figs 10, 11) demonstrates rather good correlation. Distribution of *P* and *S* anomalies obtained by these two ways are also similar, and it means that these two approaches are practically equivalent.

5.5 Images of *Qp*

Results of inversion are given in terms of *p*-wave attenuation, 1/*Qp*, at vertical and horizontal sections in Figs 14 and 15. In general, the results of inversion are similar to the images presented in (Schurr *et al.* 2003). However, there are also some differences caused by the differences in the ray paths and by the differences in parametrization methods. Note, that our approach which includes double nodes at seismic interfaces allows modelling of sharp velocity and 1/*Qp* contrasts at the interfaces and prevents from smearing of the anomalies from the crust into the mantle and vice versa.

6 INTERPRETATION AND DISCUSSION

Detailed interpretation of the tomographic images in the entire region of tomographic inversion will be published elsewhere (Sobolev & Koulakov, in preparation). Here we will indicate some more qualitative and general points and discuss in more details interpretation of our images along the cross-section at 21°S, where a lot of other geophysical observations were collected in the framework of the SFB 267 project.

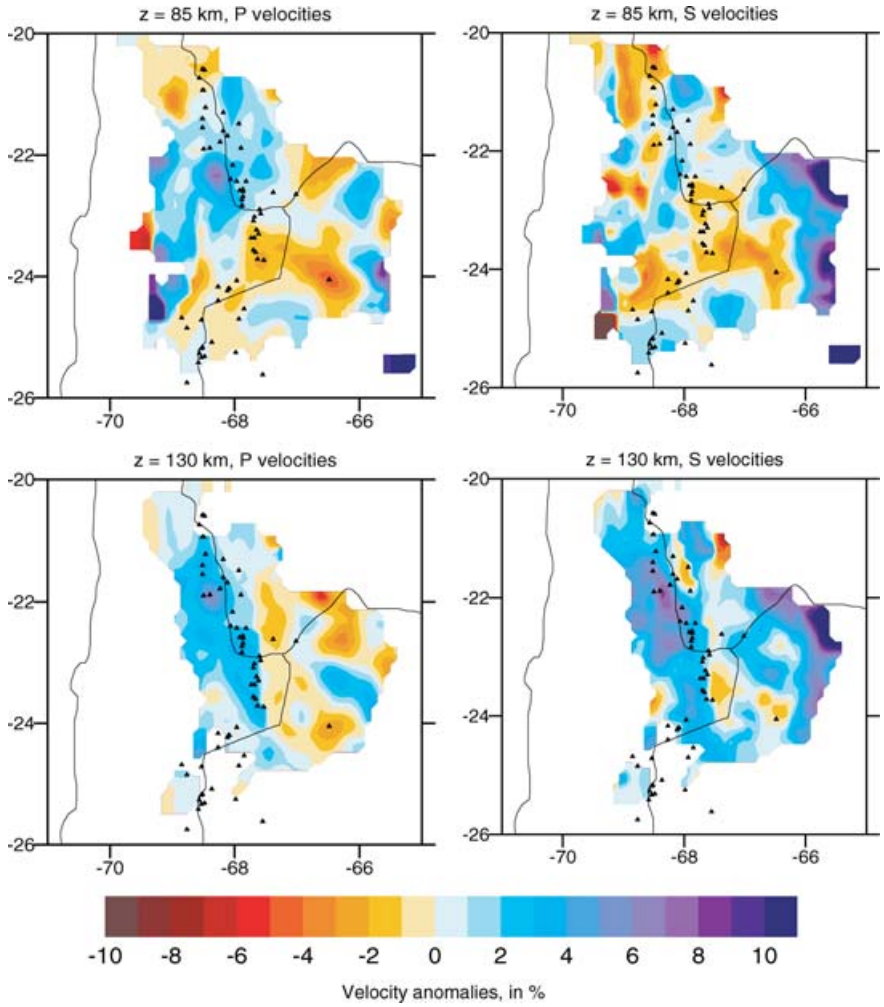

Figure 11. (*Continued.*)

In general there is good correlation between *P*- and *S*- wave anomalies in the entire region, which is not prescribed by our inversion technique. This adds credibility to the features observed in both *P*- and *S*-velocity anomalies. It also means that the most likely factors responsible for the observed anomalies are either variations of temperature and degree of partial melting, or variations of composition or all these factors together. The strongest anomalies in *P* and *S* velocities in the crust are associated with present-day volcanic arc and adjacent edge of the Altiplano plateau (Fig. 11). These anomalies are well correlated with the high seismic wave attenuation (Fig. 15), high *Vp/Vs* ratio (Fig. 12) and high electrical conductivity in the crust (Brasse *et al.* 2002). Together with strong middle-crust *P*-to-*S* conversions suggesting pronounced crustal seismic low-velocity zone in the same region (Yuan *et al.* 2000), this suggests that the middle crust in the arc and adjacent Altiplano is hot and in places partially molten.

In some places in the crust (like a region around Tuzgle volcano) correlation between *P*- and *S*- velocity anomalies fails. Thus strong negative *P*-velocity anomaly not associated with the strong negative *S*- velocity anomaly at -24°, -66°, 25–50 km depth (Fig. 11) is difficult to interpret. Note, however that resolution in *S*-velocity model in this particular region is not as good as in other parts of the imaged area. This can be concluded from analyses of the results of the odd- and even-numbers resolution test (see Fig. 8).

Our best model (based on 3-D CWS starting model) generates values of absolute seismic velocities (see lower section of Fig. 6) compatible with expected composition and possible range of temperatures in the crust and upper mantle. For instance most of *P* velocities in the mantle wedge are between 7.7 and 8.3 km s^{-1}, which corresponds to the typical peridotite with temperature between 800° and 1400° (Sobolev *et al.* 1996, 1997). In the upper mantle *P*- and *S*-velocity anomalies are generally well correlated, and in most cases they also anticorrelate with *Vp/Vs* ratio and attenuation. This type of correlation indicates important influence of temperature variations and allows quantifying the magnitude of such variations using direct inversion of the seismic data for distribution of temperature within the mantle wedge (Sobolev and Koulakov, in preparation). Such analyses suggests that alternating positive and negatives velocity anomalies in the mantle wedge (see Fig. 10) can be interpreted in terms of varying temperatures, possibly associated with variable thickness of the mantle lithosphere of the upper plate, being at different stages of delamination. The domains of low velocities in the mantle wedge almost reaching thick crust in the Eastern Cordillera and Northern Puna may be interpreted as regions of completed mantle lithosphere delamination processes. The adjacent (to the east) domains of high velocities in the mantle wedge at the depth of 100–150 km bounded from above by the low velocities in the eastern part may indicate active delamination processes.

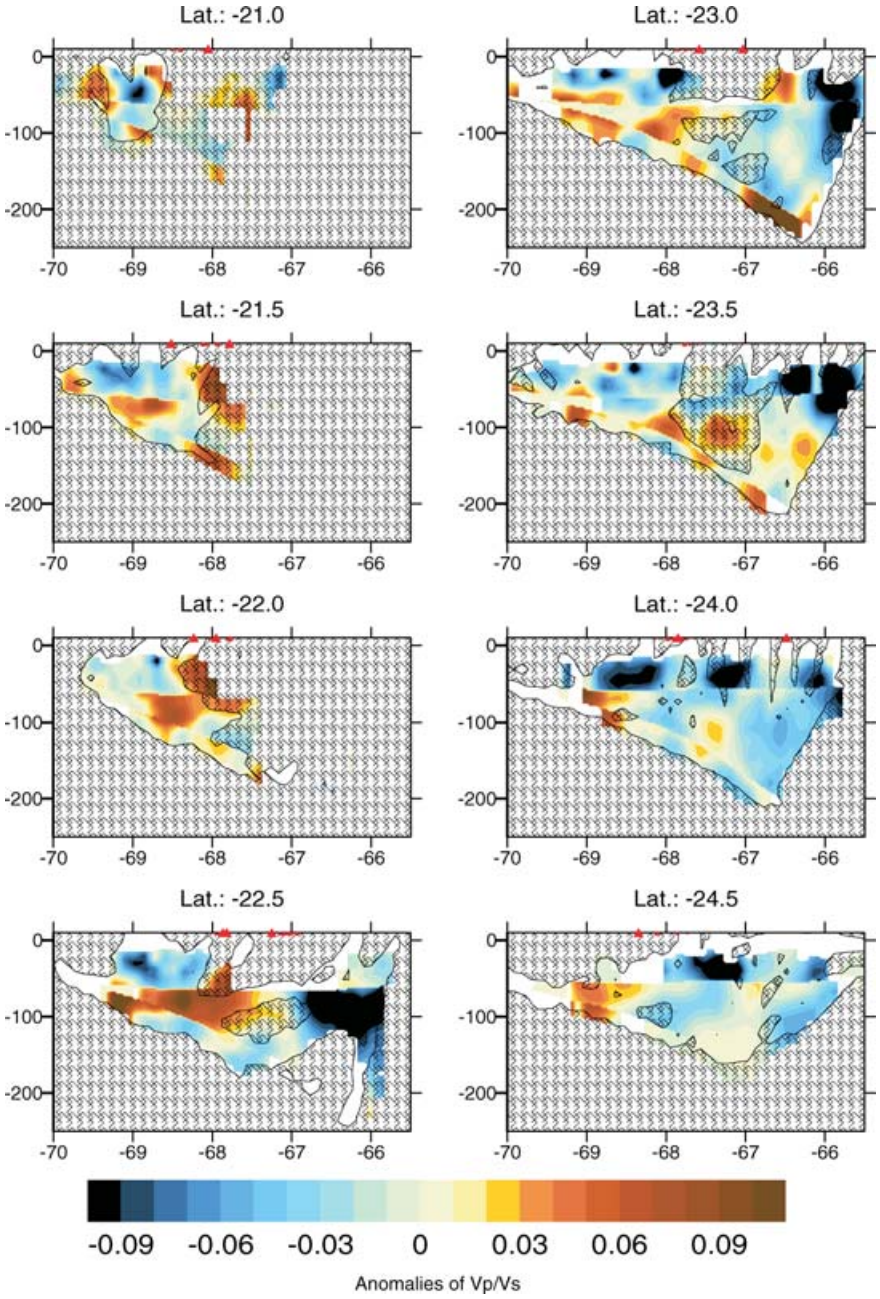

Figure 12. Vertical sections of the *Vp/Vs* perturbations with respect to the 3-D-Complex starting model from 5 iterations of direct inversion for *Vp* and *Vp/Vs*. Non-shaded area mean the areas with sufficient density of *S* rays (0.5 of average density).

The forearc basins like Salar de Atacama block, indicated by high velocities in the crust and uppermost mantle have likely mafic lower crust and relatively low temperatures.

Now let us focus at the line at 21°S, where a lot of other geophysical observations were collected in the framework of the SFB 267 project. Haberland *et al.* (2003) presented the results of seismic attenuation tomography together with the magneto-telluric sounding images (Brasse *et al.* 2002). Alternation of *Qp* factor is observed in the crust along the profile 21°S: low attenuation under the forearc, narrow zone of high *Qp* under the arc, low *Qp* in the back arc and extremely high attenuation under Altiplano plateau. The similar alternation is observed in the images of electrical resistivity derived from the magnetotelluric sounding. Our tomographic images (both *P* and *S*, see Fig. 14) fit well to these results: low-velocity zones correspond to high attenuation and low electrical resistivity. This correlation supports high temperature–partial melt explanation for the Altiplano crustal anomaly. This result is also in accordance with the receiver function data for the Altiplano (Yuan *et al.* 2000).

Among the most exiting observations at 21°S profile is strong reflector imaged by the near vertical reflection method (ANCORP Group 1999, 2003; Yoon *et al.* 2003) which likely correspond to the top of the Nasca subducted plate (Nasca reflector, Fig. 16). This reflector has exceptional strength at the depth range of 60–80 km. Further to the west this reflector disappears and instead a bright reflection anomaly called Quebrada-Blanca bright spot (QBBS) is imaged in the crust at 20–30 km depth (Fig. 16). The QBBS is located above the main earthquake cluster within the slab in the depth interval between 100 and 120 km. Location of the QBBS is

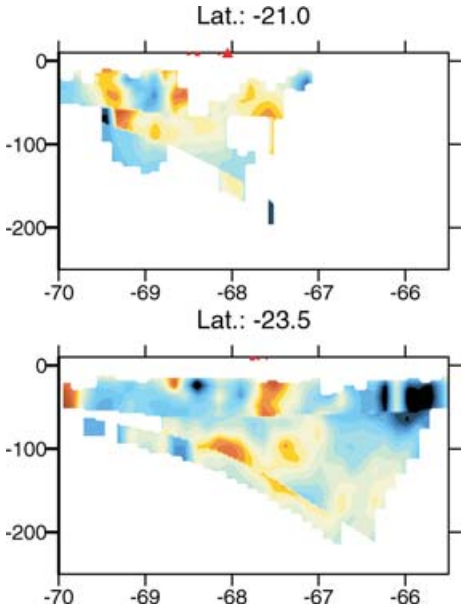

Figure 13. Two sections of the *Vp/Vs* perturbations derived after five iterations of inversion for *Vp* and *Vs*.

consistent with low-velocity anomalies in both *P* and *S* waves in our model as well as with high seismic attenuation and low electric resistivity (Haberland *et al.* 2003). Moreover, from our images we infer that QBBS has clear connection with the 80–90 km depth (Fig. 16), e.g. with the deepest end of the Nazca reflector. Resolution test (Fig. 9) completely excludes the possibility that this connection could result from the down smearing of the anomaly from the upper crust. Interestingly, *low* seismic velocities anomalies correlate with *high Vp/Vs* ratio (Fig. 16b).

We suggest the following explanation for the observed anomaly at the QBBS and its connection to the mantle. We assume that the low-velocity anomalies connect the QBBS to the Nasca reflector. In our model the Nazca reflector represents felsic continental crustal rocks eroded and transported by the slab down to the depth of 80 km. Extremely sheared, low-velocity felsic rocks cause powerful near vertical seismic reflections. At the depth of 80–90 km, high temperature and possibly also partial melting of the wet felsic rocks (at temperature *ca.* 650° C) result in decrease of viscosity of the felsic rocks and they begin to rise diapirically. Additional motivation for that could be intensified fluid flux from the slab above the earthquake cluster. Destabilization of the layer of the eroded rocks explains disappearance (or strength reduction) of the Nasca reflector at *ca.* 80 km depth. The diapires are rising to the crust and stop at the depth where temperature is becoming too low (rocks viscosity too high) to permit uplift of the diapires. Felsic composition (high quarts contents) of the rising rocks explains low seismic velocity anomalies associated with decreased *Vp/Vs* ratio. Note that *Vp/Vs* ratio in the felsic rocks is lower than in mafic crustal rocks and ultramafic mantle rocks (e.g. Sobolev & Babeyko 1994). Low electrical conductivity and low seismic attenuation in the crust and upper mantle in this area may be explained by relatively low degree of partial melting of rising felsic rocks, such that melt inclusions do not form connected clusters, until diapires rise to their upper point at 20–30 km depth.

In this scenario the QBBS is the upper limit of the diapiric flow, where the felsic melt inclusions may become interconnected and melts are segregated and accumulated in thin layer, and low *P*- and *S*- velocity anomalies linking QBBS and Nasca reflector represent uprising partially molten felsic diapires. Melts and felsic rocks imbedded within more mafic crustal rocks in forearc cause exceptional reflective properties of the QBBS and small size of this body precludes its elector–magnetic imaging.

7 CONCLUSIONS

In areas with complex velocity structure the inversion problem is **non-unique**. Different models can provide the same variance reduction. The rms is important but not the only one criterion for selection of the best model. Our 'CWS 3-D model' constrained only on the basis of other *a priori* information, without considering the observed traveltimes, provides however the same rms as the '1-D-Minimal model'. At the same time, it gives much more reasonable values of absolute *P* and *S* velocities, which could be interpreted in terms of temperature and other petrophysical parameters.

The nature of seismic anomalies in the slab, mantle wedge and crust can be different. That is why, to avoid smearing of anomalies from one zone to another, it is important that the parametrization of the model allowed sharp contrasts at the main boundaries. In our work it is realized by introducing doubled nodes at the interfaces.

Test with independent inversion of two data subsets seems to be very important for evaluation of contribution of the random noise in the data to the final results. Comparison of the images obtained by this way can be used for evaluation of sizes and amplitudes of trustworthy patterns. In our data set good resemblance of the images testify to relatively good quality of data and high reliability of the obtained anomalies.

Inversion for *Vp* and *Vp/Vs* performed in this study gives practically equivalent results as the independent *Vp* and *Vs* inversion, that is an evidence for self-consistency of the model, which is not obvious taking into account number of free parameters at the inversion.

Inversion for *Qp* parameter is independent from the velocity inversion and it gives generally consistent images with the *Vp* and *Vs* results. Some difference of *Qp* distribution in our study from the results by Schurr *et al.* (2003) obtained for the same data set, is mostly due to different way of parametrization which in our case allows modelling sharp contrasts at main interfaces.

The resulting tomographic images show complicated, essentially 3-D structure in the lithosphere and asthenosphere. The forearc basins like Salar de Atacama block are indicated by high velocities in the crust suggesting mafic composition and relatively low temperatures. Low velocities under Altiplano are apparently associated with the partial melting in the crust. Tuzgle volcano is probably associated with the asthenospheric upwelling. High velocities in the mantle wedge at the depth of 100–150 km bounded from above by the low velocities in the eastern part may indicate active delamination processes.

Quebrada Blanca bright spot may be linked to the Nasca reflector, suggesting the same nature of these two features: felsic crustal rocks eroded and transported by the slab (Nasca reflector) and then diapirically uplifted and trapped in the middle crust (Quebrada Blanca bright spot).

ACKNOWLEDGMENTS

This research was made with financial support of the SFB 267 Project.

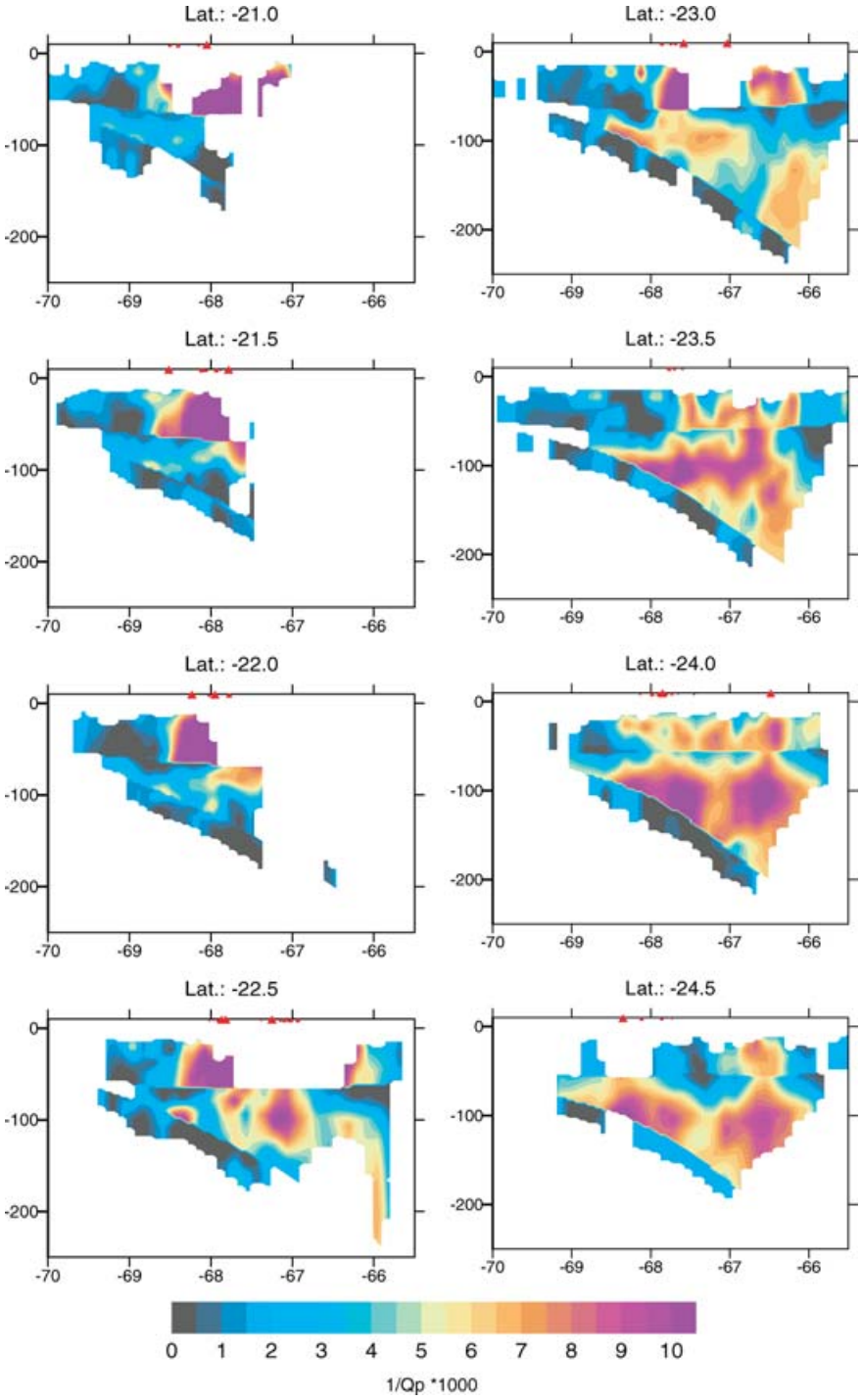

Figure 14. Results of inversion for the *P*-wave attenuation (1/*Qp*), vertical sections.

REFERENCES

ANCORP Research Group, 1999. Seismic reflection image of the Andean subduction zone reveals offset of intermediate-depth seismicity into oceanic mantle, *Nature*, **349,** 341–344.

ANCORP Working Group, 2003. Seismic imaging of an active continental margin—the central Andes (ANCORP '96). *Journ. Geophys. Res.,* **108,** doi:10.1029/2002JB001771.

Babeyko, A., Sobolev, S.V., Trumbull, R., Oncken, O. & Lavier, L., 2002. Numerical models of crustal scale convection and partial melting beneath the Altiplano-Puna plateau, *Earth planet. Sci. Lett.,* **199,** 373–388.

Baumond, D., Paul, A., Beck, S. & Zandt, G., 1999. Strong crustal heterogeneity in the Bolivian Altiplano as suggested by attenuation of Lg waves, *J. geophys. Res.,* **104,** 20 287–20 305.

Baumond, D., Paul, A., Zandt, G., Beck, S. & Pedersen, H., 2002. Lithospheric structure of the central Andes based on surface wave dispersion, *J. geophys. Res.,* **107**(B12), 2371, doi:10.1029/2001JB000345.

Brasse, H., Lezaeta, P., Rath, V., Schwalenberg, K., Soyer, W. & Haak, V., 2002. The Bolivian Altiplano conductivity anomaly, *Geophys. Res.,* **107**(B5), doi:10.1029/2001JB000391.

Beck, S. & Zandt, G., 2002. The nature of orogenic crust in the central Andes, *J. geophys. Res.,* **107**(B10), 2230, doi:10.1029/2000JB000124.

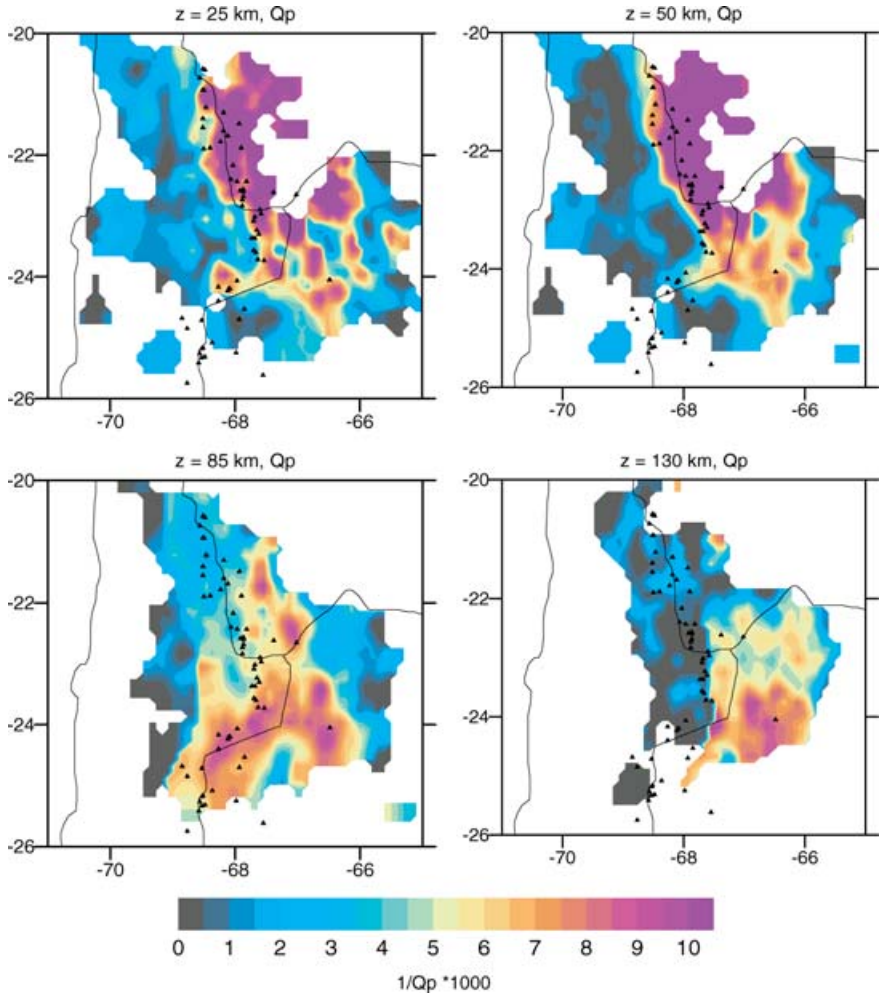

Figure 15. Results of inversion for the *P*-wave attenuation (1/*Qp*), horizontal sections.

Beck, S., Zandt, G., Myers, S., Wallace, T., Silver, P. & Drake, L., 1996. Crustal thickness variation in the central Andes, *Geology,* **24,** 407–410.

Cerveny, V., Molotkov, I. & Psencik, I., 1977. *Ray method in seismology*, University of Karlova Press, Prague, Czechoslovakia. Reutter, K.-J., Scheuber, E. & Wigger, O.-J., pp. 23–48, Springer, Berlin, Heidelberg, New York, 1994.

Crosson, R.S., 1976. Crustal structure modeling of earthquake data 1, simultaneous least square estimation of hypocenter and velocity parameter, *J. geophys. Res.,* **81,** 3036–3046.

DeMets, C., Gordon, R., Argus, D. & Stein, S., 1990. Current plate motions, *Geophys. J. Int.,* **101,** 425–478.

de Silva, S.L. & Francis, P.W., 1991. *Volcanoes of the Central Andes*, Springer Verlag, Heidelberg, pp. 199–212 (Appendix II).

Dorbath, C. & Masson, F., 2000. Composition of the crust and upper-mantle in the Central Andes (19°30′S) inferred from P wave velocity and Poisson's ratio, *Tectonoph,* **327,** 213–223.

Dorbath, C., Granet, M., Poupinet, G. & Martinez, C., 1993. A teleseismic study of the Altiplano and the Eastern Cordiliera in northern Bolivia: new constrains on a lithospheric model, *J. geophys. Res.,* **98,** 9825–9844.

Funck, T., Louden, K.E., Wardle, R.J., Hall, J., Hobro, J.W., Salisbury, M.H. & Muzzatti, A.M., 2000. Three-dimensional structure of the Torngat origin (NE Canada) from active seismic tomography, *J. geophys. Res.,* **105**(B10), 23 403–23 420.

Giese, P., Scheuber, E., Schilling, F., Schnitz, M. & Wigler, P., 1999. Crustal thickening precesses in the Central Andes and the different natures of the Moho-discontinuity, *Journal of South American Earth Sciences,* **12,** 201–220.

Götze, H.-J., Lahmeyer, B., Schmidt, S. & Strunk, S., 1994. The lithospheric structure of the Central Andes (20–26 S) as inferred from interpretation of regional gravity, in *Tectonics of the Central Andes—Structure and Evolution of an Active Continental Margin*, eds Reutter, K.-J., Scheuber, E. & Wigger, P., Springer, Berlin, Heidelberg, New York.

Graeber, F. & Asch, G., 1999. Three-dimensional models of *P*-wave velocity and P-to-S ratio in the southern central Andes by simultaneous inversion of local earthquake data, *J. geophys. Res.,* **104,** 20 237–20 256.

Haberland, C. & Rietbrock, A., 2001. Attenuation tomography in the western central Andes: a detailed insight into the structure of a magmatic arc, *J. geophys. Res.,* **106,** 11 151–11 167.

Haberland, C., Riebrock, A., Schurr, B. & Brasse, H., 2003. Coincident anomalies of seismic attenuation and electrical resistivity beneath the southern Bolivian Altiplano plateau, *Geophys. Res. Lett.,* **30**(18), 1923, doi:10.1029/2003GL017492.

Hauksson, E. & Haase, J.S., 1997. Three-dimensional Vp and *Vp/Vs* velocity models of the Los Angeles basin and central transverse ranges, *California, J. geophys. Res.,* **102**(B3), 5423–5453.

Husen, S., Kissling, E. & Flueh, E., 2000. Local earthquake tomography of shallow subduction in north Chile: A combined onshore and offshore study, *J. geophys. Res.,* **105,** 28 183–28 198.

Kissling, E., Ellsworth, W., Eberhard-Phillips, D. & Kradolfer, U., 1994. Initial reference models in local earthquake tomography, *J. geophys. Res.,* **99,** 19 635–19 646.

Koulakov, I.Yu., 1998. 3D tomographic structure of the upper mantle beneath the central part of Eurasian continent, *Geophys. J. Int.,* **133**(2), 467–489.

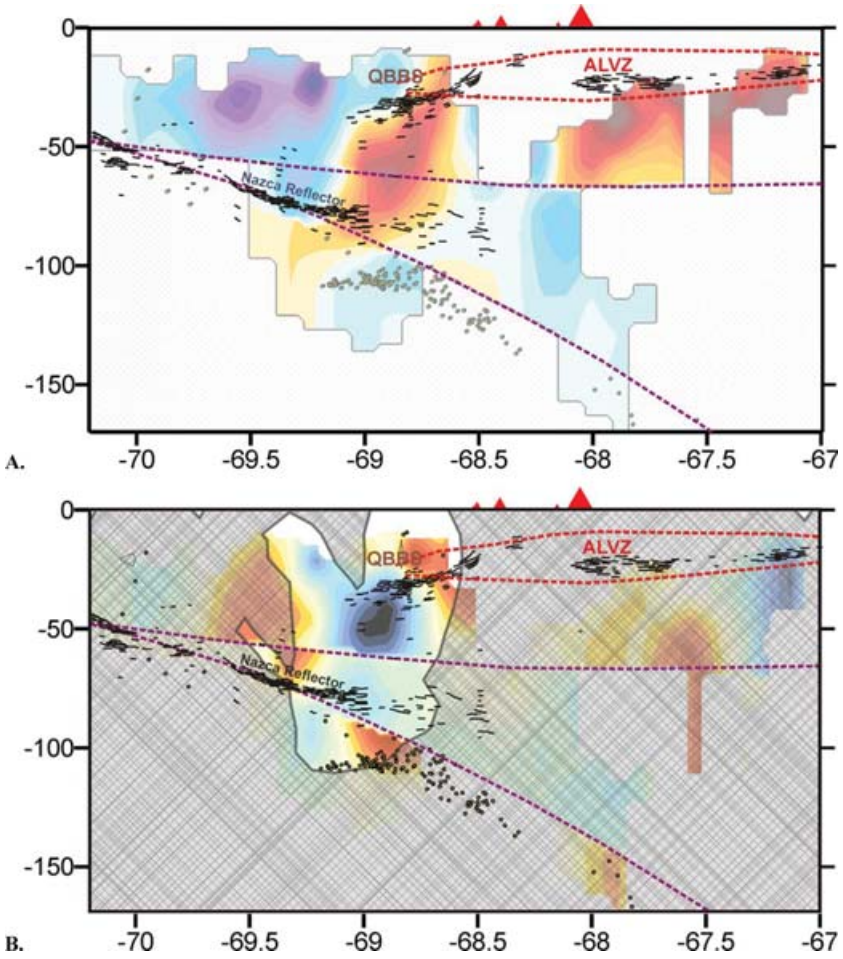

Figure 16. Comparison of the tomographic image of *P*-wave anomalies (A) and *Vp/Vs* ratio (B) at a section of 21° latitude with results of near vertical reflection studies by Yoon *et al.* (2003), ANCORP Group (2003). QBBS: Quebrada Blanca bright spot, ALVZ: Altiplano low-velocity zone.

Koulakov, I., Tychkov, S., Bushenkova, N. & Vasilevskiy, A., 2002. Structure and dynamics ovf the upper mantle beneath the Alpine-Himalayan orogenic belt, from teleseismic tomography, *Tectonophysics,* **358,** 77–96.

Leidig, M. & Zandt, G., 2003. Modeling of highly anisotropic crust and application to the Altiplano-Puna volcanic complex of the central Andes, *J. geophys. Res.,* **108,** 2014.

Myers, S., Beck, S., Zandt, G. & Wallace, T., 1998. Lithospheric-scale structure across the Bolivian Andes from tomographic images of velocity and attenuation for P and S waves, *J. geophys. Res.,* **103,** 21 233–21 252.

Nakajima, J., Matsuzawa, T., Hasegawa, A. & Zhao, D., 2001. Three-dimensional structure of Vp, Vs and Vp/Vs beneath northeastern Japan: Implication for arc magmatism and fluids, *J. geophys. Res.,* **106,** 21 843–21 857.

Nolet, G., 1987. Seismic wave propation and seismic tomography, in *Seismic Tomography, With Application, in Global Seismology and Exploration Geophysics*, pp. 1–27, ed. Nolet, G.D., Reidel, Norwell, Massachusetts.

Paige, C.C. & Saunders, M.A., 1982. LSQR: An algorithm for sparse linear equations and sparse least squares, *ACM trans. Math. Soft.,* **8,** 43–71.

Patzwahl, R., Mechie, J., Schulze, A. & Giese, P., 1999. 2D-velocity models of the Nazca plate subduction zone between 20 and 25 degrees S from wide-angle seismic measurements during the CINCA95 project, *J. geophys. Res.,* **104,** 7293–7317.

Pavlis, G.L. & Booker, J.R., 1980. The mixed Discrete-Continuous inverse problem: application to the simultaneous Determination of earthquake hypocenters and velocity structure, *J. geophys. Res.,* **85,** 4801–4810.

Rietbrock, A. & Scherbaum, F., 1998. The GIANT analysis system, *Seism. Res. Lett.,* **69,** 40–45.

Scheuber, E., Bogdanic, T., Jensen, A. & Reutter, K.-J., 1994. Tectonic development of the north Chilean Andes in relation to plate convergence and magmatism since the Jurassic, in *Tectonics of the Southern Central Andes*, pp. 121–139, eds Reutter, K.-J., Scheuber, E. & Wigger, P., Springer-Verlag, New York.

Schmidt, M. & Poli, S., 1998. Experimentally based water budgets for dehydrating slabs and consequences for arc magma generation, *Earth planet. Sci. Lett.,* **163,** 361–379.

Schmitz, M., 1994. A balanced model of the southern central Andes, *Tectonics,* **13,** 484–492.

Schurr, B., Asch, G., Rietbrock, A., Kind, R., Pardo, M., Heit, B. & Monfret, T., 1999. Seismicity and average velocity beneath the Argentine Puna, *Geophys. Res. Lett.,* **26,** 3025–3028.

Schurr, B., 2001. Seismic structure of the Central Andean Subduction Zone from Local Earthquake Data, STR01/01, *PhD thesis,* GFZ-Potsdam.

Schurr, B., Asch, G., Rietbrock, A., Trumbull, R. & Haberland, C., 2003. Complex patterns of fluid and melt transport in the central Andean subduction zone revealed by attenuation tomography, *Earth planet. Sci. Lett.,* **215,** 105–119.

Sobolev, S. & Babeyko, A., 1994. Modeling of mineralogical composition and elastic wave velocities in anhydrous magmatic rocks, *Surv. Geophys.,* **15,** 515–544.

Sobolev, S.V., Zeyen, H., Stoll, G., Werling, F., Altherr, R. & Fuchs, K., 1996. Upper mantle temperatures from teleseismic tomography of French Massif Central including effects of composition, mineral reactions, anharmonicity, anelasticity and partial melt, *Earth planet. Sci. Lett.,* **139,** 147–163.

Sobolev, S.V., Zeyen, H., Granet, M., Achauer, U., Bauer, C., Werling, F., Altherr, R. & Fuchs, K., 1997. Upper mantle temperature and lithosphere–asthenosphere system beneath the French Massif Central constrained by seismic, gravity, petrologic and thermal observations, *Tectonophysics,* **275,** 143–164.

Swenson, J., Beck, S. & Zandt, G., 2000. Crustal structure of the Altiplano from broadband regional waveform modeling: Implication for the composition of thick continental crust, *J. geophys. Res.,* **105,** 607–621.

Thurber, C., 1993. Local earthquake tomography: Velocities and vp/vs-theory, in *Seismic Tomography: theory and practice*, pp. 563–583, eds Iyer, H. & Hirahara, K., Chapman and Hall, London.

Um, J. & Thurber, 1987. A fast algorithm for two-point seismic ray tracing, *Bull. seism. Soc. Am.,* **77,** 972–986.

Van der Sluis, A. & van der Vorst, H.A., 1987. Numerical solution of large, sparse linear algebraic systems arising from tomographic problems, in *Seismic tomography*, pp. 49–83, ed. Nolet, G., Reidel, Dortrecht.

Virieux, J., Farra, V. & Madariaga, R., 1988. Ray tracing for earthquake location in laterally heterogeneous media, *J. geophys. Res.,* **93,** 6585–6599.

Waldhauser, F. & Ellsworth, W.L., 2000. A double-difference Earthquake location algorithm: method and application to the northern Hayward fault, California, *Bull. seis. Soc. Am.,* **90**(6), 1353–1368.

Wigger, P.J. *et al.*, 1994. Variation of the crustal structure of the southern Central Andes deduced from seismic refraction investigations, in *Tectonics of the Southern Central Andes*, pp. 23–48, eds Reutter, K.-J., Scheuber, E. & Wigger, P., Springer, Berlin.

Worner, G., Moorbath, S. & Harmon, R., 1992. Andean Ceonozoic volcanic centers reflect basement isotopic domains, *Geology,* **80,** 1103–1106.

Yoon, M., Buske, S., Lüth, S., Schulze, A., Shapiro, S.A., Stiller, M. & Wigger, P., 2003. Along-strike variations of crustal reflectivity related to the Andean subduction process, *Geophys. Res. Lett.,* **30,** 4, 1160.

Yuan, X., Sobolev, S.V., Kind, R., Onken, O. & ANDES Research group, 2000. Subduction and collision processes in the Central Andes constrained by converted seismic phases, *Nature,* **408,** 958–961.

Yuan, X., Sobolev, S.V. & Kind, R., 2002. Moho topography in the central Andes and its geodynamic implications, *Earth planet. Sci. Lett.,* **199,** 389–402.

APPENDIX A: SHOOTING RAY TRACER

We have developed an algorithm of two-points ray tracing in complex 3-D media. The velocity distribution should be parametrized smoothly in several domains separated by smooth interfaces. The interfaces and 3-D velocity distribution within each domain is parametrized in a set of nodes (not necessarily regular). To smooth the 3-D velocity fields and 2-D interfaces, we have developed rather fast and universal algorithm for smooth interpolation. It is based on 1-D smoothing by flattening of edges of a linearly interpolated function with polynomials of third order, which is expanded to 2-D and 3-D cases.

To construct a ray between two fixed points in 3-D space (two-points ray problem) we develop the adjustment method of tracing which is based on construction of a series of rays with defined initial parameters in starting point (one-point ray tracing). The method of solution of the one-point ray problem is based on numerical integration of the ray equations (Cerveny *et al.* 1977):

$$\begin{cases} dP_x = -\dfrac{\partial V}{\partial x}\dfrac{dS}{V^2}, & dx = VP_x dS \\ dP_y = -\dfrac{\partial V}{\partial y}\dfrac{dS}{V^2}, & dy = VP_y dS \\ dP_z = -\dfrac{\partial V}{\partial z}\dfrac{dS}{V^2}, & dz = VP_z dS \end{cases},$$

with initial values of coordinates: $x = x^0$, $y = y^0$, $z = z^0$ and direction: $P(x^0, y^0, z^0) = P^0$.

Where P is a slowness vector (direction of the ray); $V(x, y, z)$ is velocity distribution; dS is the integration step. The ray path after crossing interfaces is computed on the basis of the Snell law: refraction:

$$P_i = P_i^0 - \left(P_i^0 N_i - \sqrt{V_2^{-2} - V_1^{-2} + P_i^0 N_i}\right)$$

reflection:

$$P_i = P_i^0 - 2\left(P_i^o N_i\right) N_i.$$

Where P^0 is initial slowness vector, P is slowness vector after refraction/reflection; N is normal vector of the surface in point of intersection with the ray; V_1 and V_2 are velocities in opposite sides of the surface.

A specific feature of the algorithm is automatic determination of length of the integration step dS depending on velocity change

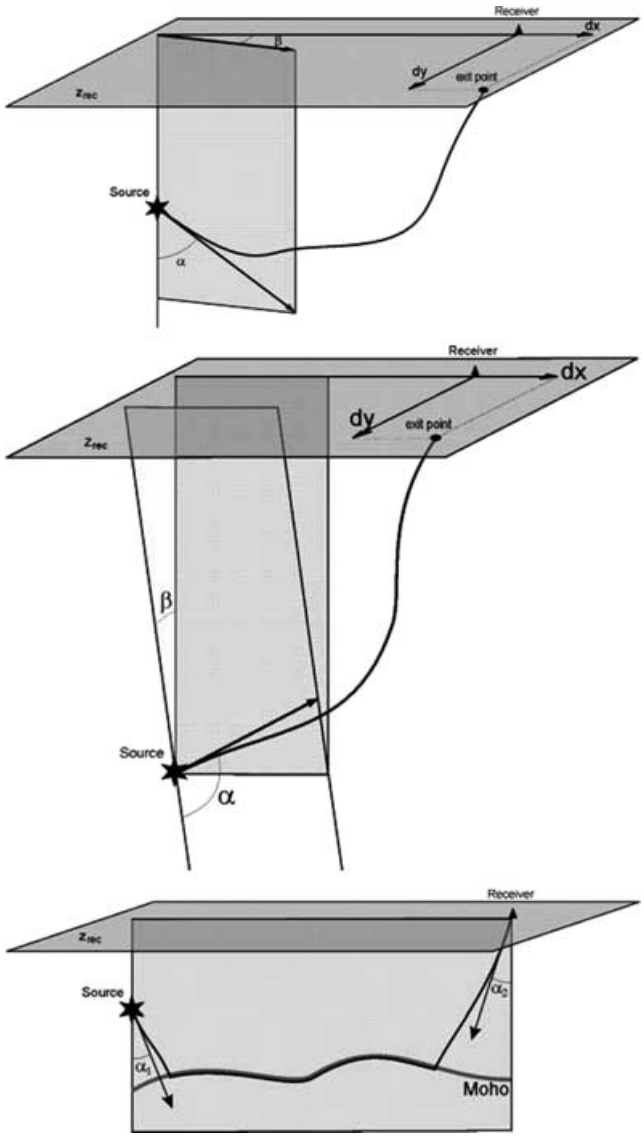

Figure 17. To the grounds of the shooting algorithm for three cases of mutual distribution of a source and receiver: (a) when the horizontal distance is greater than the depth of source; (b) when the source is deep and (c) when the source is in the crust and the head wave travels along the Moho.

around the current point. In addition, if the ray passes near an interface with velocity jump, the length of dS is set so that the next point gets as close to the interface as possible. This optimization allows significant reduction of calculation time in complex 3-D models.

Two-points ray problem is solved iteratively, with the starting parameters of the following ray tracing according to results of previous steps. We distinguish three cases depending on relative position of a source and receiver (Fig. 17) with different calculation schemes. First scheme (Fig. 17a) is realized when the horizontal distance between source and receiver is greater than the source depth. In this case the dipping angle α and azimuth β play the role of adjusting parameters. For the first ray, the starting parameters are estimated in a 1-D velocity medium, which fits the expected 3-D distribution best. The end of the ray is set in a point where it crosses the depth level corresponding to the receiver. In cylindrical coordinates with the centre in the source point, distance r_1 and azimuth ϕ_1 of the end point are computed. The next ray is shot with starting parameters

$$\alpha_2 = \alpha_1 + (\partial\alpha/\partial r)\, dx$$
$$\beta_2 = \beta_1 - dy/x_{\mathrm{rec}}.$$

The starting parameters for the next iterations are determined by solution of system of liner equations using the results of the previous shots.

The second scheme is used when the depth of the source is greater than the epicentral distance (Fig. 17b). In this case the ray starts in a plane R which passes trough the source and is parallel to the line between projection of the source at the surface and receiver. Axes x, y, z are defined as shown in the Fig. 17(b). The adjusting parameters are α, angle between x-axe and initial direction of the ray, and β, the angle between planes R and XOZ. The output point of a ray is defined as intersection with the plane XOY. The starting parameters of the rays are adjusted according to position of the output point with respect to the receiver point (dx, dy).

Source location in the crust is particular case because of non-stability of shooting ray tracing. In fact, when a part of a ray passes below the Moho, small variations of initial parameters cause brutal changes of the output, and the adjusting method does not work. That is why we propose an approximate algorithm of tracing for this case (Fig. 17c). First of all we try to find an exact solution with the use of one of the two schemes mentioned above. If the iterative procedure does not lead to a solution, it probably means that this is a refracted ray (*Pn* or *Sn*) that travels below Moho. In this case the ray consists of three parts. The parts corresponding to the partitions of the ray in the crust are constructed with the use of the one-point tracing procedure described above. The initial horizontal angle corresponds to the azimuth between the source and receiver. The dipping angle is evaluated from 1-D model, which corresponds to the refracted wave. The part of the ray below the crust is constructed as a line which follows the bottom side of Moho. The traveltime along this path is computed taking into account the velocity distribution under Moho.